Electronic Supplementary Information

A Series of Isostructural Polyoxometalate-Based Metal–Organic Frameworks of 3,5-Bis(1′,2′,4′-triazol-1′-yl)pyridine: Synthesis, Structures and Electrocatalytic Properties

Tinghui Xie[a], Xinfang Wang[a], Tingting Cao[a], Zuogang Huang[a,b,*], Huaguang Yu[a,b,*]

[a] *Key Laboratory of Optoelectronic Chemical Materials and Devices, Ministry of Education, College of Optoelectronic Materials and Technology, Jianghan University, Wuhan 430056, P. R. China*
[b] *State Key Laboratory of Precision Blasting, Jianghan University, Wuhan 430056, P. R. China*

*Corresponding author. Tel.: +86-27-84225508; fax: +86-27-84225508.
Email addresses: hzg19@jhun.edu.cn (Zuogang Huang), hgyu@jhun.edu.cn (Huaguang Yu)

Preprint submitted to Dalton Transactions *November 25, 2024*

Contents

List of Tables

List of Figures

1. Material and Methods

Cobalt nitrate ($Co(NO_3)_2{\cdot}6H_2O$), nickel nitrate ($Ni(NO_3)_2{\cdot}6H_2O$), zinc nitrate ($Zn(NO_3)_2{\cdot}6H_2O$), and ammonium molybdate tetrahydrate ($(NH_4)_6Mo_7O_{24}{\cdot}4H_2O$) were used as received from Sinopharm Chemical Reagent Corporation. The ligand 3,5-bis(1′,2′,4′-triazol-1′-yl)pyridine (btap) was prepared according to the literature method [1, 2]. Powder X-ray diffraction (PXRD) data were collected using a Panalytical X'pert diffractometer with Cu Kα radiation (λ = 1.54178 Å). Fourier transform infrared (FT-IR) spectroscopy was performed using a Bruker Tensor 27 FTIR spectrometer. Thermogravimetric analysis (TGA) were carried out using a TA Instruments SDT Q600 thermal analyzer under a constant stream of dry nitrogen gas (flow rate 20 ml min^{-1}) over the temperature range of 40 – 800 °C and at a heating rate of 20 K min^{-1}. Elemental analyses (C, H, and N) were carried out on an Elementar vario EL cube elemental analyzer. A Renishaw *InVia* Raman spectrometer was used to record Raman spectra. Transmission electron microscopy (TEM) images were obtained on a FEI Tecnai F20 transmission electron microscope. A Hitachi SU-8010 scanning electron microscope was used to ensure the morphology of the catalyst (SEM images), equipped with an energy-dispersive X-ray spectroscopy (EDXS). A Shimadzu Kratos Analytical AXIS SUPRA$^+$ X-ray photoelectron spectrometer equipped with a micro-focus Al Kα X-ray source was employed to perform X-ray photoelectron spectroscopy (XPS) measurements.

2. Synthesis

2.1. Synthesis of POMOFs

Synthesis of $[Co^{II}_2(btap)_2(\beta\text{-}Mo_8O_{26})(H_2O)_4]{\cdot}4H_2O$ (compound **1** or Co-POMOF). A mixture of $Co(NO_3)_2{\cdot}6H_2O$ (73.0 mg, 0.25 mmol), $(NH_4)_6Mo_7O_{24}{\cdot}4H_2O$ (62.0 mg, 0.05 mmol), and btap (11.0 mg, 0.05 mmol) in 5 ml H_2O with 3 – 4 drops of 1 mol l^{-1} HCl solution was sealed in a 25 ml Teflon® reactor, which was heated at 120 °C for 3 days. After being cooled to room temperature, large block pink crystals of compound **1** were obtained in about 50 % yield (based on btap). Elemental analysis results for $C_{18}H_{30}Co_2Mo_8N_{14}O_{34}$: Calc. (%), C 11.55, H 1.62, N 10.47; Found (%), C 11.23, H 1.95, N 10.25. FT-IR (KBr pellet, cm^{-1}): 3620 (w), 3561 (m), 3479 (w), 3279 (m), 3134 (w), 3055 (w), 2971 (w), 1649 (m), 1597 (m), 1526 (s), 1448 (m), 1368 (m), 1295 (m), 1217 (m), 1171 (w), 1136 (m), 1047 (w), 993 (w), 954 (s), 912 (s), 826 (m), 719 (s), 651 (m), 561 (w), 465 (w).

Synthesis of $[Ni^{II}_2(btap)_2(\beta\text{-}Mo_8O_{26})(H_2O)_4]{\cdot}4H_2O$ (compound **2** or Ni-POMOF). The compound **2** was prepared similarly to that of compound **1**, but $Ni(NO_3)_2{\cdot}6H_2O$ (73.0 mg, 0.25 mmol) was used instead of $Co(NO_3)_2{\cdot}6H_2O$. Large block green crystals of compound **2** were obtained in a 42 % yield based on btap. Elemental analysis results for $C_{18}H_{30}Ni_2Mo_8N_{14}O_{34}$: Calc. (%), C 11.55, H 1.62, N 10.48; Found (%), C 11.18, H 1.88, N 10.22. FT-IR (KBr pellet, cm^{-1}): 3623 (w), 3576 (w), 3490 (w), 3322 (m), 3135 (w), 3057 (w), 1645 (m), 1549 (m), 1525 (s), 1452 (s), 1368 (m), 1304 (m), 1168 (m), 1136 (m), 1077 (w), 1052 (w), 999 (m), 955 (s), 910 (s), 826 (m), 718 (m), 665 (m), 640 (m), 559 (w), 519 (w), 461 (w).

Synthesis of $[Zn^{II}_2(btap)_2(\beta\text{-}Mo_8O_{26})(H_2O)_4]\cdot 4H_2O$ (compound **3** or Zn-POMOF). The compound **3** was prepared similarly to that of the compound **1**, but $Zn(NO_3)_2\cdot 6H_2O$ (73.0 mg, 0.25 mmol) was used instead of $Co(NO_3)_2\cdot 6H_2O$. Large colorless block crystals of Zn-POMOF were obtained in a 20 % yield based on btap. Elemental analysis results for $C_{18}H_{30}Zn_2Mo_8N_{14}O_{34}$: Calc. (%), C 11.47, H 1.60, N 10.40; Found (%), C 11.12, H 1.91, N 10.28. FT-IR (KBr pellet, cm^{-1}): 3621 (w), 3561 (w), 3485 (w), 3297 (m), 3135 (w), 3053 (w), 2968 (w), 1781 (w), 1712 (w), 1645 (m), 1597 (m), 1528 (s), 1450 (m), 1371 (m), 1297 (m), 1218 (m), 1173 (m), 1138 (m), 1046 (w), 994 (m), 954 (s), 911 (s), 829 (m), 719 (m), 650 (m), 561 (m), 518 (w), 464 (w).

The morphology of the crystals of (a) **1**, (b) **2** and (c) **3** was presented in Fig. S1.

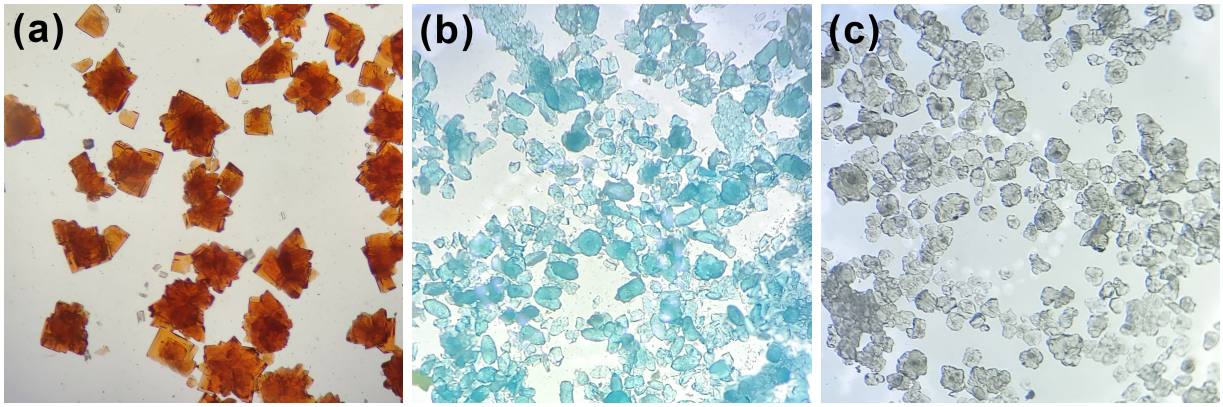

Figure S1: The morphology of the crystals of (a) **1**, (b) **2** and (c) **3**.

2.2. Synthesis of Co/Ni-POMOF-T

Co/Ni-POMOFs were calcined in a traditional tubular furnace at a rate of 5 °C min^{-1} and maintained for 2 h in argon atmosphere at different temperature to obtain Co and Ni-POMOF-T series (T = 700, 800, 900 and 1000 °C). Co-POMOF pyrolyzed at 700, 800, 900 and 1000 °C, were named Co-POMOF-700, Co-POMOF-800, Co-POMOF-900 and Co-POMOF-1000, respectively. Ni-POMOF heated at 700, 800, 900 and 1000 °C were denoted as Ni-POMOF-700, Ni-POMOF-800, Ni-POMOF-900 and Ni-POMOF-1000, respectively.

3. Structure Determination of Single Crystals

Suitable single crystals of the compounds **1**, **2** and **3** were selected for single crystal X-ray diffraction analyses. Crystallographic data were collected on a Bruker AXS SMART APEX II CCD single crystal X-ray diffractometer with graphite monochromated Mo Kα radiation (λ = 0.71073 Å). The APEX 2 program was used to collect the frames of data, index the reflections and determine the lattice parameters; SAINT [3] was used for the integration of the intensities of the reflections and scaling; SADABS [4] was used for the absorption correction; and SHELXTL [5, 6] was used for the space-group determination. Structures were solved by direct method or Patterson method with SHELXT program [7]

and refined by the full matrix least-square method on the basis of F^2 using SHELXL-2014 program [8, 9] contained in OLEX2 suite graphical user interface [10]. All non-hydrogen atoms were refined with anisotropic displacement parameters during the final cycles. All hydrogen atoms of the organic molecule were placed by geometrical considerations and added to the structure factor calculation. The crystallographic information files (CIFs) were compiled with OLEX2. These data can be obtained free of charge from The Cambridge Crystallographic Data Centre (CCDC). CCDC 2373986 (for **1**), 2373987 (for **2**), and 2373988 (for **3**) contained the supplementary crystallographic data for this paper. The PLATON program enabled for the checking for additional symmetry elements. The overall structures of the compounds were analyzed using TOPOS software [11]. The formula for **1**, **2** and **3** were determined by single crystal structure. Crystallographic figures were generated with Diamond 3.1e software [12]. The detailed bond lengths and bond angles for these compounds were tabulated in Tables S2 – S7.

Table S1: Crystallographic data and structure refinement parameters for compounds **1** – **3**

	1	**2**	**3**
Empirical formula	$C_{18}H_{30}Co_2Mo_8N_{14}O_{34}$	$C_{18}H_{30}Ni_2Mo_8N_{14}O_{34}$	$C_{18}H_{30}Zn_2Mo_8N_{14}O_{34}$
Formula weight	1871.94	1871.50	1884.82
Temperature (K)	296(2)	296(2)	296(2)
Crystal system	orthorhombic	orthorhombic	orthorhombic
Space group	*Pbca* (no. 61)	*Pbca* (no. 61)	*Pbca* (no. 61)
a (Å)	15.5814(7)	15.7082(12)	15.5823(6)
b (Å)	16.4046(8)	16.2936(12)	16.4405(7)
c (Å)	17.8430(8)	17.7195(13)	17.8841(7)
α (°)	90.00	90.00	90.00
β (°)	90.00	90.00	90.00
γ (°)	90.00	90.00	90.00
Volume (Å^3)	4560.8(4)	4535.2(6)	4581.6(3)
Z	4	4	4
Density (calc.) (g cm^{-3})	2.726	2.741	2.733
λ (Mo Kα) (Å)	0.71073	0.71073	0.71073
Absorption coefficient (μ mm^{-1})	2.949	3.064	3.259
F (000)	3592.0	3600.0	3616.0
$2\theta_{max}$ (°)	57	55	55
Goodness-of-fit on F^2	1.191	1.238	1.046
R_{int}	0.0510	0.0454	0.0533
R_1/wR_2 ($I > 2\sigma(I)$) [a]	0.0183, 0.0458	0.0170, 0.0419	0.0225, 0.0453
R_1/wR_2 (all data)	0.0193, 0.0462	0.0179, 0.0422	0.0319, 0.0480

[a] $R_1 = \frac{\sum||F_o|-|F_c||}{\sum|F_o|}$; $wR_2 = [\frac{\sum w(F_o{}^2-F_c{}^2)^2}{\sum w(F_o{}^2)^2}]^{1/2}$.

*3.1. Crystal Structure of Compound **1***

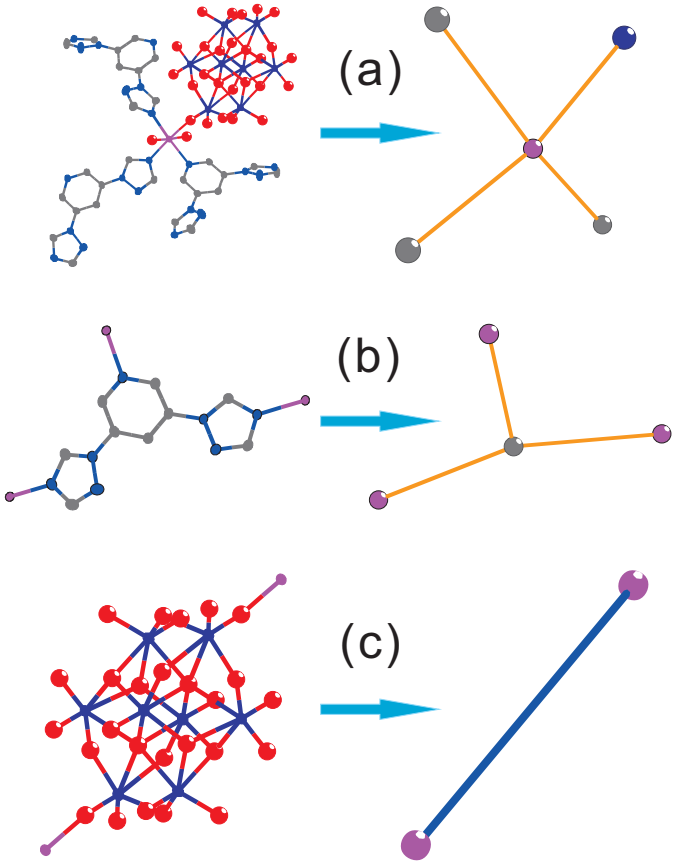

Figure S2: Abstracting the underlying topology in compound **1**. (a) Co1 cation is regarded as a 4-connected node. (b) 3,5-bis(1′,2′,4′-triazol-1′-yl)pyridine ligand can be considered as a 3-connected node. (c) The $(\beta\text{-}Mo_8O_{26})^{4-}$ anion is considered as linkage.

Table S2: Selected bond lengths (Å) of compound **1**

bond	**length (Å)**	**bond**	**length (Å)**
Mo3–O8	1.9599(17)	Co1–N7#2	2.140(2)
Mo3–O11	1.9325(17)	Co1–N4#3	2.230(2)
Mo3–O15#1	2.4065(16)	Co1–O1	2.0534(19)
Mo3–O15	2.0969(16)	O8–Mo4#1	2.2989(17)
Mo3–O9	1.6857(18)	O11–Mo2#1	2.3407(17)
Mo3–O10	1.7613(18)	O15–Mo3#1	2.4065(16)
Mo2–O8	2.0028(16)	O10–Mo1#1	2.2475(18)
Mo2–O11#1	2.3406(17)	N1–C2	1.324(3)
Mo2–O15	2.3495(16)	N1–C1	1.360(4)
Mo2–O5	1.8995(18)	N7–Co1#4	2.140(2)
Mo2–O6	1.6973(19)	N7–C8	1.359(3)
Mo2–O7	1.688(2)	N7–C9	1.320(3)
Mo1–O15	2.4691(16)	N3–N2	1.372(3)
Mo1–O14	1.9224(18)	N3–C2	1.332(3)
Mo1–O5	1.9045(18)	N3–C3	1.420(3)
Mo1–O3	1.7264(18)	N4–Co1#5	2.230(2)
Mo1–O10#1	2.2475(18)	N4–C6	1.341(3)
Mo1–O4	1.685(2)	N4–C7	1.338(3)
Mo4–O8#1	2.2989(17)	C6–C5	1.381(3)
Mo4–O11	1.9923(17)	N2–C1	1.312(4)
Mo4–O15	2.3234(16)	C8–N6	1.312(3)
Mo4–O14	1.8895(18)	C7–C3	1.383(3)
Mo4–O12	1.708(2)	N5–C9	1.335(3)
Mo4–O13	1.6956(19)	N5–C5	1.419(3)
Co1–O3	2.1624(18)	N5–N6	1.364(3)
Co1–N1	2.129(2)	C5–C4	1.384(3)
Co1–O2	2.0353(19)	C4–C3	1.382(3)

[1] #1: 1 – X, 1 – Y, 1 – Z; #2: 3/2 – X, 2 – Y, – 1/2 + Z; #3: + X, 3/2 – Y, – 1/2 + Z; #4: 3/2 – X, 2 – Y, 1/2 + Z; #5: + X, 3/2 – Y, 1/2 + Z.

Table S3: Selected angles (°) of compound **1**

angle	(°)	**angle**	(°)
O8–Mo3–O15	79.37(7)	N1–Co1–N4#2 [1]	174.88(8)
O8–Mo3–O15#1 [1]	76.85(6)	O2–Co1–O3	89.58(8)
O11–Mo3–O8	150.37(7)	O2–Co1–N1	89.93(9)
O11–Mo3–O15#1 [1]	78.18(6)	O2–Co1–N7#3 [1]	91.56(8)
O11–Mo3–O15	79.47(7)	O2–Co1–N4#2 [1]	89.10(8)
O15–Mo3–O15#1 [1]	76.39(6)	O2–Co1–O1	176.57(8)
O9–Mo3–O8	101.28(9)	N7#3–Co1–O3 [1]	174.28(7)
O9–Mo3–O11	102.86(9)	N7#3–Co1–N4#2 [1]	91.77(8)
O9–Mo3–O15	100.75(8)	O1–Co1–O3	87.16(8)
O9–Mo3–O15#1 [1]	176.79(8)	O1–Co1–N1	89.14(8)
O9–Mo3–O10	104.37(9)	O1–Co1–N7#3 [1]	91.79(8)
O10–Mo3–O8	93.65(8)	O1–Co1–N4#2 [1]	91.53(8)
O10–Mo3–O11	96.74(8)	Mo3–O8–Mo2	108.71(8)
O10–Mo3–O15	154.81(7)	Mo3–O8–Mo4#1 [1]	111.56(7)
O10–Mo3–O15#1 [1]	8.45(7)	Mo2–O8–Mo4#1 [1]	103.72(7)
O8–Mo2–O11#1 [1]	71.44(6)	Mo3–O11–Mo2#1 [1]	111.16(7)
O8–Mo2–O15	72.63(6)	Mo3–O11–Mo4	109.10(8)
O11#1–Mo2–O15 [1]	72.11(6)	Mo4–O11–Mo2#1 [1]	102.58(7)
O5–Mo2–O8	145.81(7)	Mo3–O15–Mo3#1 [1]	103.60(6)
O5–Mo2–O11#1 [1]	84.26(7)	Mo3–O15–Mo2	92.64(6)
O5–Mo2–O15	77.28(7)	Mo3#1–O15–Mo1 [1]	91.55(5)
O6–Mo2–O8	101.29(8)	Mo3–O15–Mo1	164.85(8)
O6–Mo2–O11#1 [1]	87.56(8)	Mo3–O15–Mo4	92.52(6)
O6–Mo2–O15	159.68(8)	Mo2–O15–Mo3#1 [1]	95.92(6)
O6–Mo2–O5	101.31(9)	Mo2–O15–Mo1	85.40(5)
O7–Mo2–O8	96.03(9)	Mo4–O15–Mo3#1 [1]	96.41(6)
O7–Mo2–O11#1 [1]	164.33(9)	Mo4–O15–Mo2	165.12(8)
O7–Mo2–O15	95.50(8)	Mo4–O15–Mo1	85.97(5)
O7–Mo2–O5	102.72(9)	Mo4–O14–Mo1	118.11(9)
O7–Mo2–O6	104.51(10)	Mo2–O5–Mo1	118.49(9)
O14–Mo1–O15	73.66(6)	Mo1–O3–Co1	168.91(11)
O14–Mo1–O10#1 [1]	76.64(7)	Mo3–O10–Mo1#1 [1]	120.81(9)
O5–Mo1–O15	74.20(6)	C2–N1–Co1	127.34(18)
O5–Mo1–O14	144.68(7)	C2–N1–C1	103.1(2)
O5–Mo1–O10#1 [1]	78.57(7)	C1–N1–Co1	129.45(17)
O3–Mo1–O15	94.11(7)	C8–N7–Co1#4 [1]	126.06(16)
O3–Mo1–O14	97.76(9)	C9–N7–Co1#4 [1]	129.59(17)
O3–Mo1–O5	98.77(8)	C9–N7–C8	103.3(2)
O3–Mo1–O10#1 [1]	163.19(8)	N2–N3–C3	120.1(2)

Continued on next page

Table S3 – continued from previous page

angle	(°)	angle	(°)
O10#1–Mo1–O15 [1]	69.14(6)	C2–N3–N2	109.7(2)
O4–Mo1–O15	159.77(9)	C2–N3–C3	130.1(2)
O4–Mo1–O14	101.65(9)	C6–N4–Co1#5 [1]	115.65(15)
O4–Mo1–O5	103.39(10)	C7–N4–Co1#5 [1]	125.33(16)
O4–Mo1–O3	106.07(10)	C7–N4–C6	118.3(2)
O4–Mo1–O10#1 [1]	90.65(9)	N4–C6–C5	122.1(2)
O8#1–Mo4–O15 [1]	72.59(6)	C1–N2–N3	102.3(2)
O11–Mo4–O8#1 [1]	72.54(6)	N6–C8–N7	114.7(2)
O11–Mo4–O15	72.94(6)	N1–C2–N3	110.1(2)
O14–Mo4–O8#1 [1]	84.82(7)	N4–C7–C3	121.8(2)
O14–Mo4–O11	147.19(7)	N2–C1–N1	114.7(2)
O14–Mo4–O15	77.86(7)	C9–N5–C5	129.2(2)
O12–Mo4–O8#1 [1]	166.07(9)	C9–N5–N6	110.14(19)
O12–Mo4–O11	96.43(9)	N6–N5–C5	120.32(19)
O12–Mo4–O15	96.34(8)	N7–C9–N5	109.7(2)
O12–Mo4–O14	101.39(9)	C6–C5–N5	119.9(2)
O13–Mo4–O8#1 [1]	86.34(8)	C6–C5–C4	120.4(2)
O13–Mo4–O11	101.26(8)	C4–C5–N5	119.6(2)
O13–Mo4–O15	158.93(8)	C8–N6–N5	102.2(2)
O13–Mo4–O14	100.63(9)	C3–C4–C5	116.6(2)
O13–Mo4–O12	104.51(10)	C7–C3–N3	120.7(2)
O3–Co1–N4#2 [1]	82.64(7)	C4–C3–N3	118.5(2)
N1–Co1–O3	92.32(7)	C4–C3–C7	120.8(2)
N1–Co1–N7#3 [1]	93.29(8)		

[1] #1: 1 – X, 1 – Y, 1 – Z; #2: 3/2 – X, 2 – Y, – 1/2 + Z;
#3: + X, 3/2 – Y, – 1/2 + Z; #4: 3/2 – X, 2 – Y, 1/2 + Z;
#5: + X, 3/2 – Y, 1/2 + Z.

3.2. Crystal Structure of Compound 2

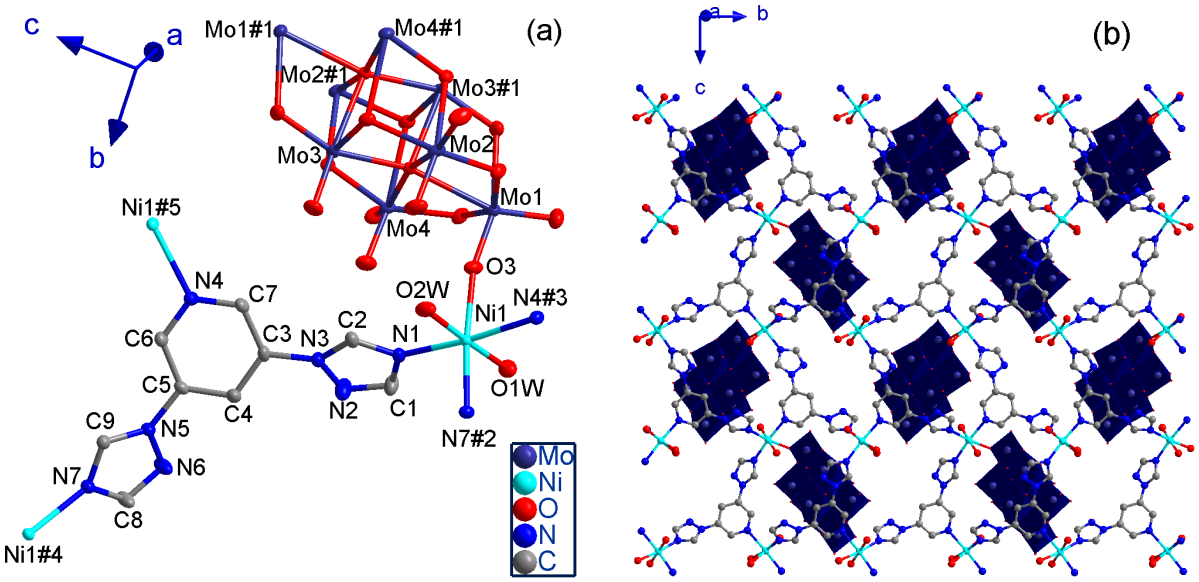

Figure S3: (a) Coordination environment (at 50 % probability level) of the Ni(II) centers in compound **2**. The hydrogen atoms and crystal water molecules are omitted for clarity. Symmetry codes for the generated atoms: #1: 2 – X, – Y, 1 – Z; #2: 3/2 – X, 1 – Y, – 1/2 + Z; #3: + X, 1/2 – Y, – 1/2 + Z; #4: 3/2 – X, 1 – Y, 1/2 + Z; #5: + X, 1/2 – Y, 1/2 + Z. (b) Perspective view of the 3D framework in compound **2** along the *a*-axis.

Table S4: Selected bond lengths (Å) of compound **2**

bond	length (Å)	bond	length (Å)
Mo3–O11	1.9554(19)	Ni1–N1	2.082(2)
Mo3–O8	1.932(2)	Ni1–O1	2.052(2)
Mo3–O15#1	2.4020(18)	Ni1–N4#3	2.179(2)
Mo3–O15	2.0945(18)	O11–Mo2#1	2.3028(19)
Mo3–O9	1.686(2)	O8–Mo4#1	2.3378(19)
Mo3–O10	1.763(2)	O15–Mo3#1	2.4019(18)
Mo4–O11	2.0031(19)	O10–Mo1#1	2.248(2)
Mo4–O8#1	2.3379(19)	N7–Ni1#4	2.083(2)
Mo4–O15	2.3550(18)	N7–C9	1.322(3)
Mo4–O14	1.901(2)	N7–C8	1.371(4)
Mo4–O13	1.698(2)	N1–C2	1.329(4)
Mo4–O12	1.687(2)	N1–C1	1.365(4)
Mo1–O5	1.922(2)	N3–N2	1.372(4)
Mo1–O3	1.730(2)	N3–C2	1.337(4)
Mo1–O15	2.4641(18)	N3–C3	1.421(3)

Continued on next page

Table S4 – continued from previous page

bond	length (Å)	bond	length (Å)
Mo1–O14	1.903(2)	N4–Ni1#5	2.179(2)
Mo1–O10#1	2.248(2)	N4–C7	1.343(3)
Mo1–O4	1.686(2)	N4–C6	1.344(3)
Mo2–O11#1	2.3027(19)	C9–N5	1.339(3)
Mo2–O8	1.994(2)	N2–C1	1.316(4)
Mo2–O5	1.887(2)	C7–C3	1.394(4)
Mo2–O15	2.3249(19)	C8–N6	1.311(4)
Mo2–O6	1.697(2)	N5–N6	1.367(3)
Mo2–O7	1.707(2)	N5–C5	1.417(3)
Ni1–O3	2.110(2)	C5–C6	1.385(4)
Ni1–N7#2	2.083(2)	C5–C4	1.385(4)
Ni1–O2	2.031(2)	C3–C4	1.381(4)

[1] #1: 1 – X, 1 – Y, 1 – Z; #2: 3/2 – X, 2 – Y, – 1/2 + Z; #3: + X, 3/2 – Y, – 1/2 + Z; #4: 3/2 – X, 2 – Y, 1/2 + Z; #5: + X, 3/2 – Y, 1/2 + Z.

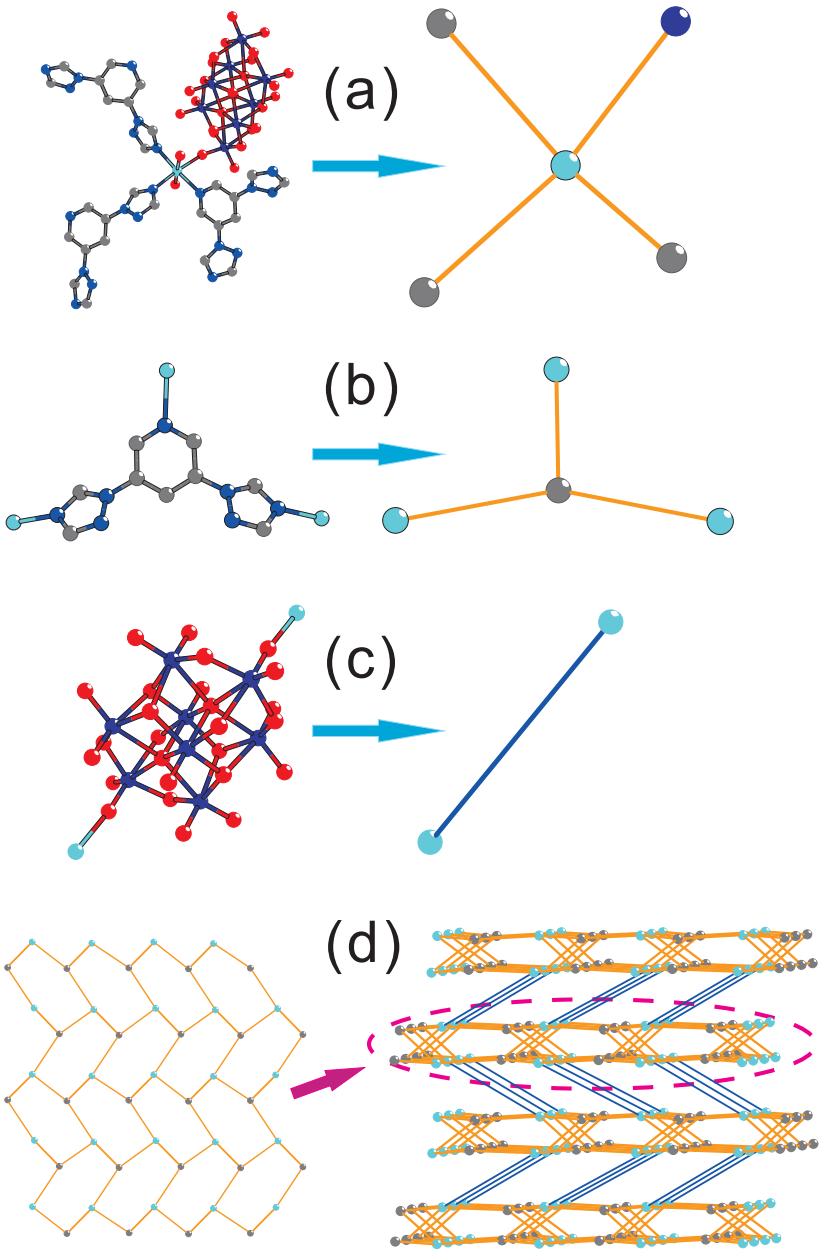

Figure S4: Abstracting the underlying topology in compound **2**. (a) Ni1 cation is regarded as a 4-connected node. (b) 3,5-Bis(1′,2′,4′-triazol-1′-yl)pyridine ligand can be considered as a 3-connected node. (c) The $(\beta\text{-}Mo_8O_{26})^{4-}$ anion is considered as linkage. (d) Schematic view of the 3D (3,4)-connected framework with the $(12)(6^3{\cdot}12^3)_2(6^3)_2$ topology in compound **2**. Color code: light green ball, 4-connected Ni(II) node; grey ball, 3-connected btap node; blue stick, $(\beta\text{-}Mo_8O_{26})^{4-}$ anion linkage.

Table S5: Selected angles (°) of compound **2**

angle	(°)	**angle**	(°)
O11–Mo3–O15	79.33(8)	O2–Ni1–O3	90.19(9)
O11–Mo3–O15#1 [1]	76.94(7)	O2–Ni1–N7#3 [1]	91.27(9)
O8–Mo3–O11	150.54(8)	O2–Ni1–N1	90.05(10)
O8–Mo3–O15	79.61(8)	O2–Ni1–O1	176.74(9)
O8–Mo3–O15#1 [1]	78.26(7)	O2–Ni1–N4#2 [1]	88.94(9)
O15–Mo3–O15#1 [1]	76.39(7)	N1–Ni1–O3	91.22(8)
O9–Mo3–O11	101.43(10)	N1–Ni1–N7#3 [1]	93.64(9)
O9–Mo3–O8	102.54(10)	N1–Ni1–N4#2 [1]	174.49(9)
O9–Mo3–O15#1 [1]	176.87(9)	O1–Ni1–O3	86.68(9)
O9–Mo3–O15	100.73(9)	O1–Ni1–N7#3 [1]	91.93(9)
O9–Mo3–O10	104.28(10)	O1–Ni1–N1	89.11(9)
O10–Mo3–O11	93.78(9)	O1–Ni1–N4#2 [1]	91.60(9)
O10–Mo3–O8	96.64(9)	Mo3–O11–Mo4	109.09(9)
O10–Mo3–O15#1 [1]	78.56(8)	Mo3–O11–Mo2#1 [1]	111.56(8)
O10–Mo3–O15	154.92(8)	Mo4–O11–Mo2#1 [1]	103.50(8)
O11–Mo4–O8#1 [1]	71.54(7)	Mo3–O8–Mo4#1 [1]	111.24(8)
O11–Mo4–O15	72.32(7)	Mo3–O8–Mo2	108.98(9)
O8#1–Mo4–O15 [1]	72.03(7)	Mo2–O8–Mo4#1 [1]	102.56(8)
O14–Mo4–O11	145.54(8)	Mo2–O5–Mo1	118.05(10)
O14–Mo4–O8#1 [1]	84.21(8)	Mo1–O3–Ni1	167.07(13)
O14–Mo4–O15	77.17(8)	Mo3–O15–Mo3#1 [1]	103.61(7)
O13–Mo4–O11	101.67(9)	Mo3–O15–Mo4	92.70(7)
O13–Mo4–O8#1 [1]	87.60(9)	Mo3–O15–Mo1	164.74(9)
O13–Mo4–O15	159.63(9)	Mo3#1–O15–Mo1 [1]	91.65(6)
O13–Mo4–O14	101.37(10)	Mo3–O15–Mo2	92.50(7)
O12–Mo4–O11	95.86(10)	Mo4–O15–Mo3#1 [1]	95.87(7)
O12–Mo4–O8#1 [1]	164.32(10)	Mo4–O15–Mo1	85.36(6)
O12–Mo4–O15	95.60(9)	Mo2–O15–Mo3#1 [1]	96.49(7)
O12–Mo4–O14	102.78(10)	Mo2–O15–Mo4	165.07(9)
O12–Mo4–O13	104.46(12)	Mo2–O15–Mo1	85.94(6)
O5–Mo1–O15	73.79(7)	Mo4–O14–Mo1	118.40(10)
O5–Mo1–O10#1 [1]	76.84(8)	Mo3–O10–Mo1#1 [1]	120.50(10)
O3–Mo1–O5	97.67(10)	C9–N7–Ni1#4 [1]	129.58(19)
O3–Mo1–O15	93.86(8)	C9–N7–C8	103.6(2)
O3–Mo1–O14	98.74(9)	C8–N7–Ni1#4 [1]	125.88(19)
O3–Mo1–O10#1 [1]	163.05(9)	C2–N1–Ni1	127.3(2)
O14–Mo1–O5	144.97(8)	C2–N1–C1	103.6(2)
O14–Mo1–O15	74.41(7)	C1–N1–Ni1	128.97(19)
O14–Mo1–O10#1 [1]	78.50(8)	N2–N3–C3	119.8(2)

Continued on next page

Table S5 – continued from previous page

angle	(°)	angle	(°)
O10#1–Mo1–O15 [1]	69.24(7)	C2–N3–N2	110.1(2)
O4–Mo1–O5	101.33(11)	C2–N3–C3	130.1(3)
O4–Mo1–O3	106.13(11)	C7–N4–Ni1#5 [1]	124.91(19)
O4–Mo1–O15	159.95(10)	C7–N4–C6	118.8(2)
O4–Mo1–O14	103.49(11)	C6–N4–Ni1#5 [1]	115.64(18)
O4–Mo1–O10#1 [1]	90.74(10)	N7–C9–N5	109.4(2)
O11#1–Mo2–O15 [1]	72.40(6)	C1–N2–N3	102.6(3)
O8–Mo2–O11#1 [1]	72.47(7)	N1–C2–N3	109.5(3)
O8–Mo2–O15	72.94(7)	N4–C7–C3	121.0(2)
O5–Mo2–O11#1 [1]	84.91(8)	N6–C8–N7	114.1(3)
O5–Mo2–O8	147.23(8)	N2–C1–N1	114.3(3)
O5–Mo2–O15	77.85(8)	C9–N5–N6	110.2(2)
O6–Mo2–O11#1 [1]	86.35(9)	C9–N5–C5	129.1(2)
O6–Mo2–O8	101.52(10)	N6–N5–C5	120.4(2)
O6–Mo2–O5	100.32(10)	C8–N6–N5	102.7(2)
O6–Mo2–O15	158.75(9)	C6–C5–N5	119.7(2)
O6–Mo2–O7	104.70(12)	C4–C5–N5	119.7(2)
O7–Mo2–O11#1 [1]	165.73(10)	C4–C5–C6	120.5(2)
O7–Mo2–O8	96.14(10)	N4–C6–C5	121.9(2)
O7–Mo2–O5	101.59(10)	C7–C3–N3	119.8(2)
O7–Mo2–O15	96.36(10)	C4–C3–N3	119.1(2)
O3–Ni1–N4#2 [1]	83.36(8)	C4–C3–C7	121.1(2)
N7#3–Ni1–O3 [1]	174.92(9)	C3–C4–C5	116.6(3)
N7#3–Ni1–N4#2 [1]	91.80(9)		

[1] #1: 1 – X, 1 – Y, 1 – Z; #2: 3/2 – X, 2 – Y, – 1/2 + Z;
#3: + X, 3/2 – Y, – 1/2 + Z; #4: 3/2 – X, 2 – Y, 1/2 + Z;
#5: + X, 3/2 – Y, 1/2 + Z.

3.3. *Crystal Structure of Compound* ***3***

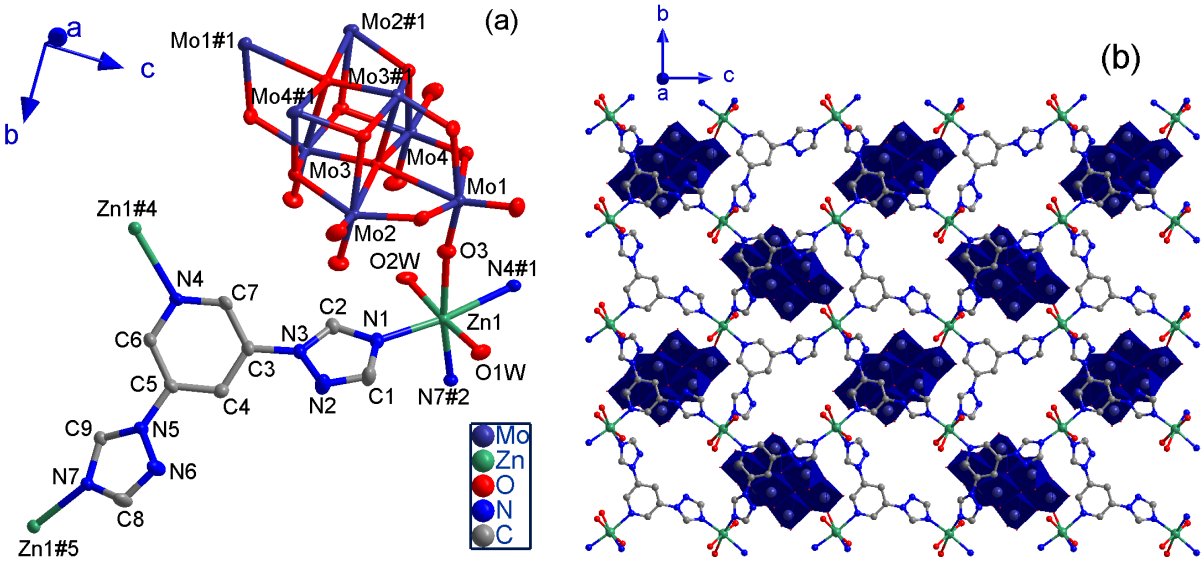

Figure S5: (a) Coordination environment (at 50 % probability level) of the Zn(II) centers in compound **3**. The hydrogen atoms and crystal water molecules are omitted for clarity. Symmetry codes for the generated atoms: #1: 2 – X, – Y, 1 – Z; #2: 3/2 – X, 1 – Y, – 1/2 + Z; #3: + X, 1/2 – Y, – 1/2 + Z; #4: 3/2 – X, 1 – Y, 1/2 + Z; #5: + X, 1/2 – Y, 1/2 + Z. (b) Perspective view of the 3D framework in compound **3** along the *a*-axis.

Table S6: Selected bond lengths (Å) of compound **3**

bond	length (Å)	bond	length (Å)
Mo3–O11	1.9554(19)	Zn1–N1	2.082(2)
Mo3–O8	1.932(2)	Zn1–O1	2.052(2)
Mo3–O15#1	2.4020(18)	Zn1–N4#3	2.179(2)
Mo3–O15	2.0945(18)	O11–Mo2#1	2.3028(19)
Mo3–O9	1.686(2)	O8–Mo4#1	2.3378(19)
Mo3–O10	1.763(2)	O15–Mo3#1	2.4019(18)
Mo4–O11	2.0031(19)	O10–Mo1#1	2.248(2)
Mo4–O8#1	2.3379(19)	N7–Zn1#4	2.083(2)
Mo4–O15	2.3550(18)	N7–C9	1.322(3)
Mo4–O14	1.901(2)	N7–C8	1.371(4)
Mo4–O13	1.698(2)	N1–C2	1.329(4)
Mo4–O12	1.687(2)	N1–C1	1.365(4)
Mo1–O5	1.922(2)	N3–N2	1.372(4)
Mo1–O3	1.730(2)	N3–C2	1.337(4)
Mo1–O15	2.4641(18)	N3–C3	1.421(3)

Continued on next page

Table S6 – continued from previous page

bond	length (Å)	bond	length (Å)
Mo1–O14	1.903(2)	N4–Zn1#5	2.179(2)
Mo1–O10#1	2.248(2)	N4–C7	1.343(3)
Mo1–O4	1.686(2)	N4–C6	1.344(3)
Mo2–O11#1	2.3027(19)	C9–N5	1.339(3)
Mo2–O8	1.994(2)	N2–C1	1.316(4)
Mo2–O5	1.887(2)	C7–C3	1.394(4)
Mo2–O15	2.3249(19)	C8–N6	1.311(4)
Mo2–O6	1.697(2)	N5–N6	1.367(3)
Mo2–O7	1.707(2)	N5–C5	1.417(3)
Zn1–O3	2.110(2)	C5–C6	1.385(4)
Zn1–N7#2	2.083(2)	C5–C4	1.385(4)
Zn1–O2	2.031(2)	C3–C4	1.381(4)

[1] #1: 1 – X, 1 – Y, 1 – Z; #2: 3/2 – X, 2 – Y, – 1/2 + Z; #3: + X, 3/2 – Y, – 1/2 + Z; #4: 3/2 – X, 2 – Y, 1/2 + Z; #5: + X, 3/2 – Y, 1/2 + Z.

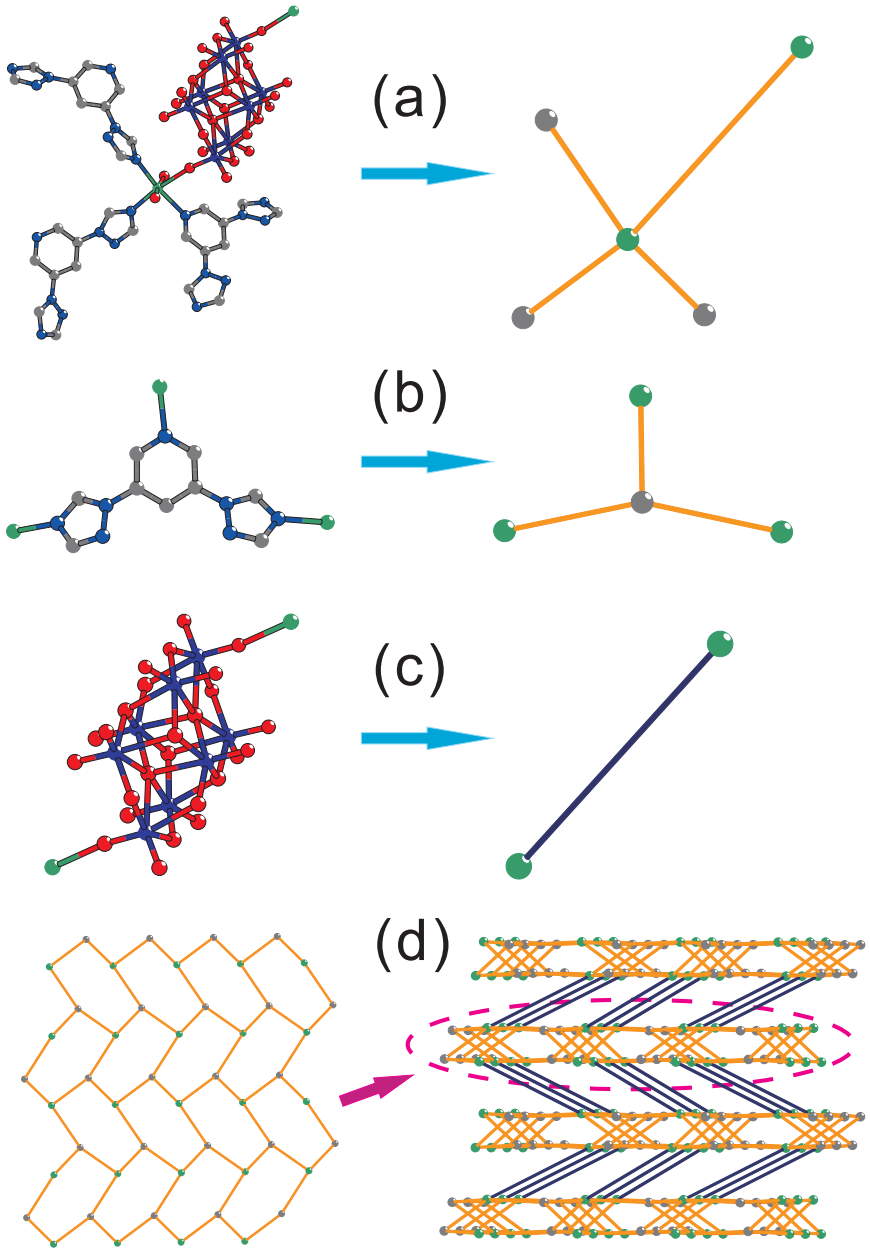

Figure S6: Abstracting the underlying topology in compound **3**. (a) Zn1 cation is regarded as a 4-connected node. (b) 3,5-Bis(1′,2′,4′-triazol-1′-yl)pyridine ligand can be considered as a 3-connected node. (c) The $(\beta\text{-}Mo_8O_{26})^{4-}$ anion is considered as linkage. (d) Schematic view of the 3D (3,4)-connected framework with the $(12)(6^3{\cdot}12^3)_2(6^3)_2$ topology in compound **3**. Color code: green ball, 4-connected Zn(II) node; grey ball, 3-connected btap node; blue stick, $(\beta\text{-}Mo_8O_{26})^{4-}$ anion linkage.

Table S7: Selected angles (°) of compound **3**

angle	(°)	**angle**	(°)
O11–Mo3–O15	79.33(8)	O2–Zn1–O3	90.19(9)
O11–Mo3–O15#1 [1]	76.94(7)	O2–Zn1–N7#3 [1]	91.27(9)
O8–Mo3–O11	150.54(8)	O2–Zn1–N1	90.05(10)
O8–Mo3–O15	79.61(8)	O2–Zn1–O1	176.74(9)
O8–Mo3–O15#1 [1]	78.26(7)	O2–Zn1–N4#2 [1]	88.94(9)
O15–Mo3–O15#1 [1]	76.39(7)	N1–Zn1–O3	91.22(8)
O9–Mo3–O11	101.43(10)	N1–Zn1–N7#3 [1]	93.64(9)
O9–Mo3–O8	102.54(10)	N1–Zn1–N4#2 [1]	174.49(9)
O9–Mo3–O15#1 [1]	176.87(9)	O1–Zn1–O3	86.68(9)
O9–Mo3–O15	100.73(9)	O1–Zn1–N7#3 [1]	91.93(9)
O9–Mo3–O10	104.28(10)	O1–Zn1–N1	89.11(9)
O10–Mo3–O11	93.78(9)	O1–Zn1–N4#2 [1]	91.60(9)
O10–Mo3–O8	96.64(9)	Mo3–O11–Mo4	109.09(9)
O10–Mo3–O15#1 [1]	78.56(8)	Mo3–O11–Mo2#1 [1]	111.56(8)
O10–Mo3–O15	154.92(8)	Mo4–O11–Mo2#1 [1]	103.50(8)
O11–Mo4–O8#1 [1]	71.54(7)	Mo3–O8–Mo4#1 [1]	111.24(8)
O11–Mo4–O15	72.32(7)	Mo3–O8–Mo2	108.98(9)
O8#1–Mo4–O15 [1]	72.03(7)	Mo2–O8–Mo4#1 [1]	102.56(8)
O14–Mo4–O11	145.54(8)	Mo2–O5–Mo1	118.05(10)
O14–Mo4–O8#1 [1]	84.21(8)	Mo1–O3–Zn1	167.07(13)
O14–Mo4–O15	77.17(8)	Mo3–O15–Mo3#1 [1]	103.61(7)
O13–Mo4–O11	101.67(9)	Mo3–O15–Mo4	92.70(7)
O13–Mo4–O8#1 [1]	87.60(9)	Mo3–O15–Mo1	164.74(9)
O13–Mo4–O15	159.63(9)	Mo3#1–O15–Mo1 [1]	91.65(6)
O13–Mo4–O14	101.37(10)	Mo3–O15–Mo2	92.50(7)
O12–Mo4–O11	95.86(10)	Mo4–O15–Mo3#1 [1]	95.87(7)
O12–Mo4–O8#1 [1]	164.32(10)	Mo4–O15–Mo1	85.36(6)
O12–Mo4–O15	95.60(9)	Mo2–O15–Mo3#1 [1]	96.49(7)
O12–Mo4–O14	102.78(10)	Mo2–O15–Mo4	165.07(9)
O12–Mo4–O13	104.46(12)	Mo2–O15–Mo1	85.94(6)
O5–Mo1–O15	73.79(7)	Mo4–O14–Mo1	118.40(10)
O5–Mo1–O10#1 [1]	76.84(8)	Mo3–O10–Mo1#1 [1]	120.50(10)
O3–Mo1–O5	97.67(10)	C9–N7–Zn1#4 [1]	129.58(19)
O3–Mo1–O15	93.86(8)	C9–N7–C8	103.6(2)
O3–Mo1–O14	98.74(9)	C8–N7–Zn1#4 [1]	125.88(19)
O3–Mo1–O10#1 [1]	163.05(9)	C2–N1–Zn1	127.3(2)
O14–Mo1–O5	144.97(8)	C2–N1–C1	103.6(2)
O14–Mo1–O15	74.41(7)	C1–N1–Zn1	128.97(19)
O14–Mo1–O10#1 [1]	78.50(8)	N2–N3–C3	119.8(2)

Continued on next page

Table S7 – continued from previous page

angle	(°)	angle	(°)
O10#1–Mo1–O15 [1]	69.24(7)	C2–N3–N2	110.1(2)
O4–Mo1–O5	101.33(11)	C2–N3–C3	130.1(3)
O4–Mo1–O3	106.13(11)	C7–N4–Zn1#5 [1]	124.91(19)
O4–Mo1–O15	159.95(10)	C7–N4–C6	118.8(2)
O4–Mo1–O14	103.49(11)	C6–N4–Zn1#5 [1]	115.64(18)
O4–Mo1–O10#1 [1]	90.74(10)	N7–C9–N5	109.4(2)
O11#1–Mo2–O15 [1]	72.40(6)	C1–N2–N3	102.6(3)
O8–Mo2–O11#1 [1]	72.47(7)	N1–C2–N3	109.5(3)
O8–Mo2–O15	72.94(7)	N4–C7–C3	121.0(2)
O5–Mo2–O11#1 [1]	84.91(8)	N6–C8–N7	114.1(3)
O5–Mo2–O8	147.23(8)	N2–C1–N1	114.3(3)
O5–Mo2–O15	77.85(8)	C9–N5–N6	110.2(2)
O6–Mo2–O11#1 [1]	86.35(9)	C9–N5–C5	129.1(2)
O6–Mo2–O8	101.52(10)	N6–N5–C5	120.4(2)
O6–Mo2–O5	100.32(10)	C8–N6–N5	102.7(2)
O6–Mo2–O15	158.75(9)	C6–C5–N5	119.7(2)
O6–Mo2–O7	104.70(12)	C4–C5–N5	119.7(2)
O7–Mo2–O11#1 [1]	165.73(10)	C4–C5–C6	120.5(2)
O7–Mo2–O8	96.14(10)	N4–C6–C5	121.9(2)
O7–Mo2–O5	101.59(10)	C7–C3–N3	119.8(2)
O7–Mo2–O15	96.36(10)	C4–C3–N3	119.1(2)
O3–Zn1–N4#2 [1]	83.36(8)	C4–C3–C7	121.1(2)
N7#3–Zn1–O3 [1]	174.92(9)	C3–C4–C5	116.6(3)
N7#3–Zn1–N4#2 [1]	91.80(9)		

[1] #1: 1 – X, 1 – Y, 1 – Z; #2: 3/2 – X, 2 – Y, – 1/2 + Z; #3: + X, 3/2 – Y, – 1/2 + Z; #4: 3/2 – X, 2 – Y, 1/2 + Z; #5: + X, 3/2 – Y, 1/2 + Z.

4. PXRD, FT-IR, Raman and TGA

Only large crystals of these POMOFs were manually selected through a microscope for characterization and electrochemical experiments. The PXRD patterns of compounds **1**, **2** and **3**, and the thermal derivatives of compounds **1** and **2**, were shown in Fig. S7, S11 and S12, respectively. All reflection peaks of compounds **1**, **2** and **3** were in good agreement with the corresponding simulated patterns without additional peaks, indicating the high purity of these compounds. The difference in intensities could be due to the preferred orientation in the powder samples.

In the FT-IR spectra of compounds **1**, **2** and **3** (Fig. S8), the peaks in a low wavenumber region of 957 – 550 cm^{-1} were assigned to Mo–O–Mo of the (β-Mo_8O_{26})$^{4-}$ polyoxoanion.

The bands at 1700 – 1300 cm^{-1} can be ascribed to the stretching vibrations of ν_{as} (C=C) and ν_{as} (C=N) in btap ligand. Vibrational absorption of C=N in btap ligand appeared near 730 cm^{-1}. The broad absorption peaks near 3400 cm^{-1} should be attributed to the vibration of ν (OH) of water molecules. The FT-IR spectra of the thermal derivatives of compounds **1** and **2** were shown in Fig. S13.

TGA in N_2 atmosphere with a heating rate of 10 °C min^{-1} was employed to investigate the thermal stability of the POMOFs. The TG curve of compound **1** (Fig. S10(a)) showed a weight loss of 7.1 % below 340 °C, attributable to the loss of lattice and coordinated water molecules, and in the range of 340 – 606 °C, 38.8 % of the weight loss could be attributed to the framework collapse of compound **1**, except that weight gain began at 606 °C, as cobalt tetroxide and cobalt trioxide gradually decomposed into denser cobalt(II) oxide. As illustrated in Fig. S10(b), the weight loss of 8.0 % within the temperature range of 56 – 350 °C can be attributed to the loss of lattice and coordination water molecules. In the temperature range of 350 – 574 °C, a weight loss of 39.2 % can be attributed to the skeleton collapse of compound **2**, resulting in the formation of molybdenum and nickel oxides as the final products. Similarly, 8.9 % of the weight loss of compound **3** (Fig. S10(c)) in the temperature range of 50 – 310 °C was attributed to the loss of water molecules, and 41.3 % of the weight loss in the range of 310 – 740 °C can be attributed to the collapse of the skeleton of compound **3**, with molybdenum oxide and zinc oxide as the final products.

The phase compositions of Co/Ni-POMOF-T were determined by PXRD. As shown in Fig. 2(a), for Co-POMOF-700, three peaks of Mo_2N (JCPDS no. 25-1626) at 37.1°, 43.1° and 62.6° were indexed to (1 1 1), (2 0 0) and (2 2 0) lattice diffraction planes. In addition, there existed another material phase of Mo_2N (JCPDS no. 24-0768), whose diffraction peaks were mainly located at 37.9° (1 1 2 plane), 40.1° (1 0 3 plane), 45.3° (0 0 4 plane), 62.6° (2 2 0 plane) and 75.3° (3 1 2 plane). The diffraction peaks of Co_3Mo_3N were mainly distributed at 35.5° (3 3 1 plane), 40.0° (4 2 2 plane), 42.6° (5 1 1 plane), 46.6° (4 4 0 plane), 55.2° (6 2 2 plane), 59.8° (5 5 1 plane), 69.7° (7 3 3 plane), 72.7° (8 2 2 plane) and 77.3° (8 4 0 plane), indicating the existed Co_3Mo_3N species in Co-POMOF-700. Furthermore, the peaks of Mo_2C were located at 34.5° (1 0 0 plane), 38° (0 0 2 plane), 39.6° (1 0 1 plane), 52.3° (1 0 2 plane), 61.9° (1 1 0 plane), 69.8° (1 0 3 plane), 75° (1 1 2 plane) and 76° (2 0 1 plane). Nevertheless, Co-POMOF-800/900/1000 were different from Co-POMOF-700, consisting of MoO_2 (JCPDS no. 25-1626), Co_2Mo_3N (JCPDS no. 09-6417) and Mo_2N (JCPDS no. 25-1626) (Fig. S11).

As shown in Fig. S12(a), Ni-POMOF-900 contained mainly four types of phases, consisting of Mo, Mo_2C, Ni_2Mo_3N and Mo_2N, in addition to small amounts of MoO_2. The diffraction peaks of Mo_2N (JCPDS no. 25-1626) were 37.17° (1 1 1 plane), 41.1° (2 0 0 plane) and 62.6° (2 2 0 plane). Futhermore, the peak intensity of Mo_2N was low, indicating a lower content. The diffraction peaks of Ni_2Mo_3N (JCPDS no. 89-4564) were mainly distributed at 30.1° (2 1 0 plane), 40.8° (2 2 1 plane), 43.1° (3 1 0 plane), 45.3° (3 1 1 plane), 59.1° (3 3 0 plane), 66° (3 3 2 plane), 69.3° (4 2 2 plane), 71° (4 3 0 plane), 72.6° (5 1 0 plane) and 77.4° (5 2 0 plane). The peaks of Mo_2C (JCPDS no. 65-8766) were located at 34.5° (1 0 0 plane), 38° (0 0 2 plane), 39.6° (1 0 1 plane), 52.3° (1 0 2 plane), 61.9° (1 1 0 plane), 69.8° (1 0 3 plane), 75° (1 1 2 plane) and 76° (2 0 1 plane). Fig. S12(b) showed the

PXRD patterns of Ni-POMOF-700/800 including MoO_2, Ni_2Mo_3N and Mo_2C. However, Ni-POMOF-1000 did not exhibit Ni_2Mo_3N phase, but only the most significant peaks of MoO_2 phase, which may be the result of the high pyrolysis temperature, causing the destruction of the phase into amorphous [13, 14]. The Si peaks (Fig. S11 and S12(b)) were from the silicon substrates used for the PXRD experiments.

The Raman spectra of compounds **1**, **2** and **3**, and the thermal derivatives of compounds **1** and **2**, were shown in Fig. S9, S14 and S15, respectively. The D_1 band generally represented the defects and distortion of the carbon layer, while the G band indicated the degree of crystalline and graphitization [15]. Besides, the deconvoluted Raman spectra also included the presence of D_5, D_4, D_3 and D_2 bands at 1210, 1420, 1510 and 1770 cm^{-1} (Table S8) [15], respectively. The integrated ratio of D_1 and G band (I_{D1}/I_G) indicated the degree of defects on the carbon layer of the composites, and I_G/I_{All} represented the degree of graphitization. Usually, the value of I_{D1}/I_G increased with the pyrolysis temperature, denoting that the degree of collapse of the compounds increased. It was observed that the I_{D1}/I_G values of the thermal derivatives corresponding to Co-POMOF at 700, 800 and 900 °C were 1.043, 1.046 and 1.073, respectively, which implies that the degree of defects did not differ much (Fig. S14(a – c)). The I_{D1}/I_G value of Co-POMOF-1000 was 0.775 (Fig. S14(d)), which showed a significant decrease in the degree of defects. The value of I_G/I_{All} for Co-POMOF-T increased with the pyrolysis temperature, which indicated that the degree of graphitization increased. However, the value of I_G/I_{All} for Ni-POMOF-900 was 0.168 (Fig. S15), suggesting that it was the least graphitized in Ni-POMOF-T.

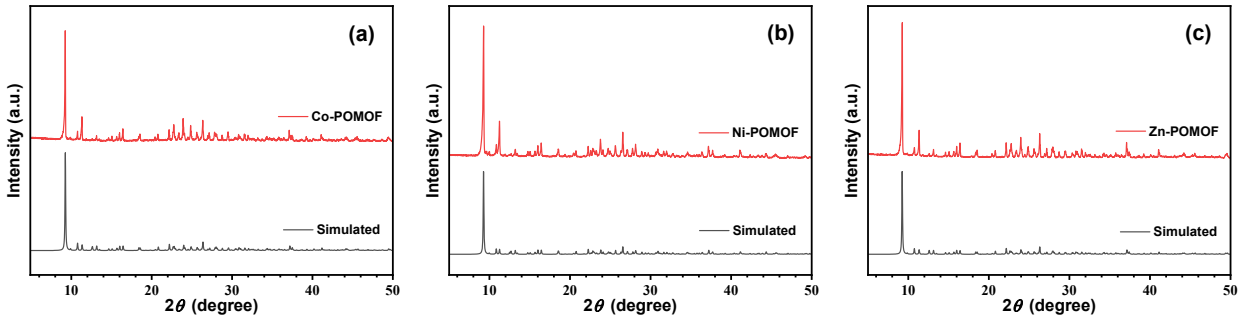

Figure S7: The experimental PXRD patterns versus the simulated patterns of compounds (a) **1**, (b) **2** and (c) **3**.

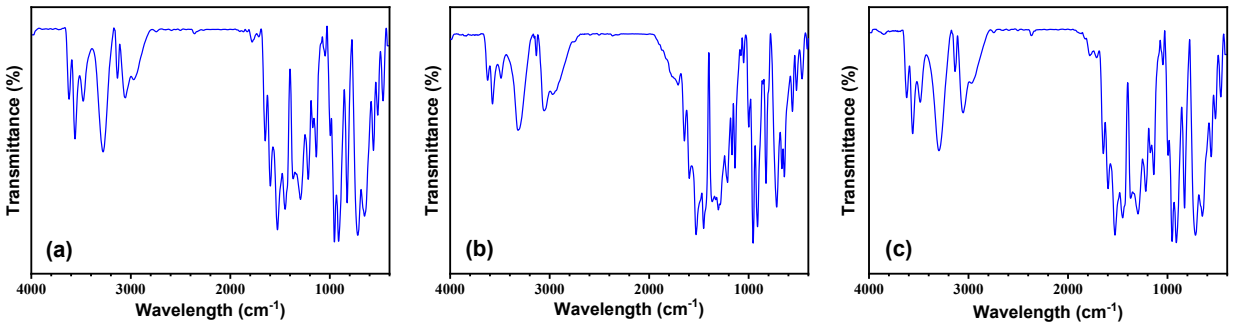

Figure S8: FT-IR spectra of (a) **1**, (b) **2** and (c) **3**.

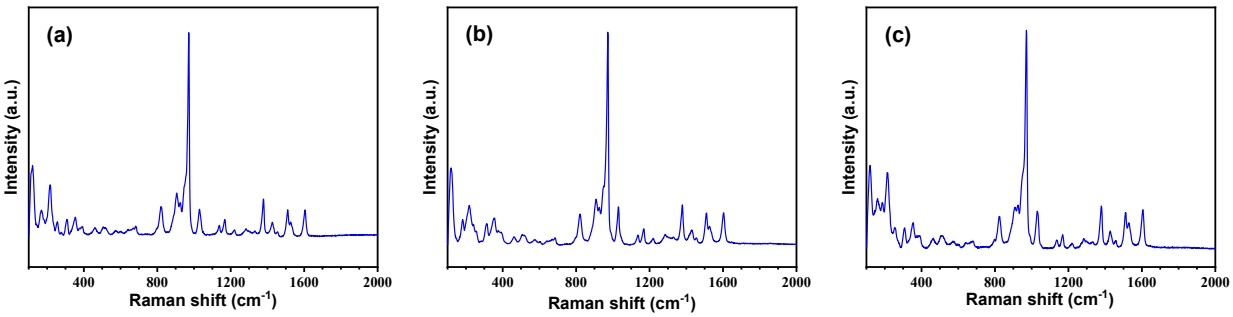

Figure S9: Raman spectra of (a) **1**, (b) **2** and (c) **3**.

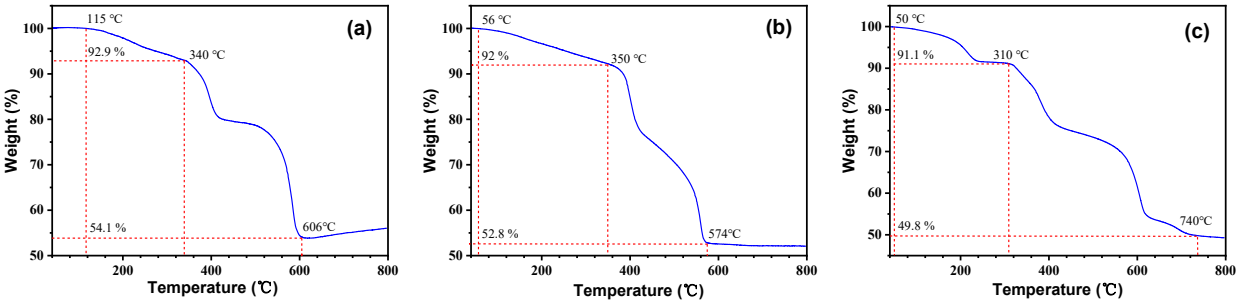

Figure S10: TG curves of (a) **1**, (b) **2** and (c) **3**.

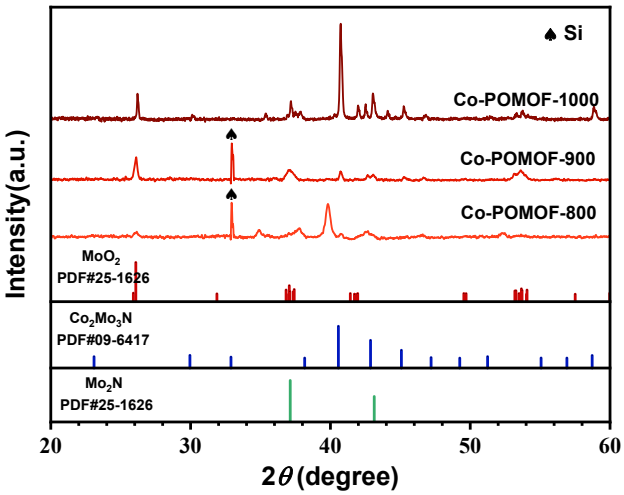

Figure S11: PXRD patterns of Co-POMOF-800, Co-POMOF-900 and Co-POMOF-1000.

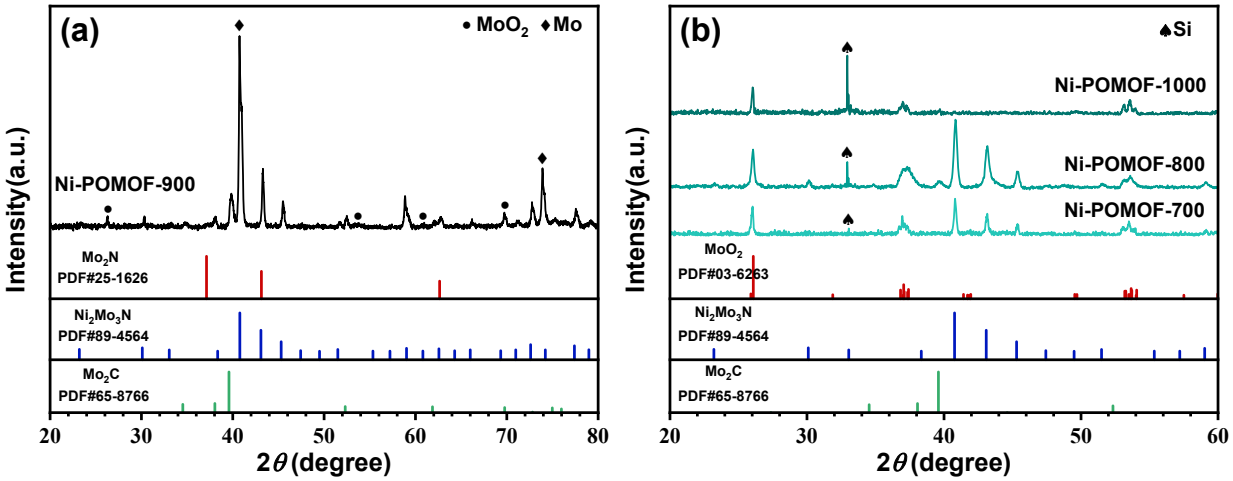

Figure S12: PXRD patterns of (a) Ni-POMOF-900, and (b) Ni-POMOF-700, Ni-POMOF-800 and Ni-POMOF-1000.

Table S8: The main functional groups determined by Raman spectroscopy and the deconvoluted Raman spectra

Band	**Raman shift (cm^{-1})**	**Vibration mode** [a]
D_5	1190 – 1210	the disordered graphitic lattice
D_1	1320 – 1340	in-plane imperfections in such as defects in graphitic lattice or graphene layers and heteroatoms [15]
D_4	1400 – 1420	amorphous carbon (Gaussian line shape)
D_3	1480 – 1510	amorphous carbon (Gaussian line shape) [16]
G	1580 – 1590	planar asymmetric stretching vibrations of C=C bonds (E_{2g} symmetry)
D_2	1750 – 1770	amorphous carbon (Gaussian line shape)

[a] Vibration mode from Co-POMOF-700/800/900 and Ni-POMOF-T.

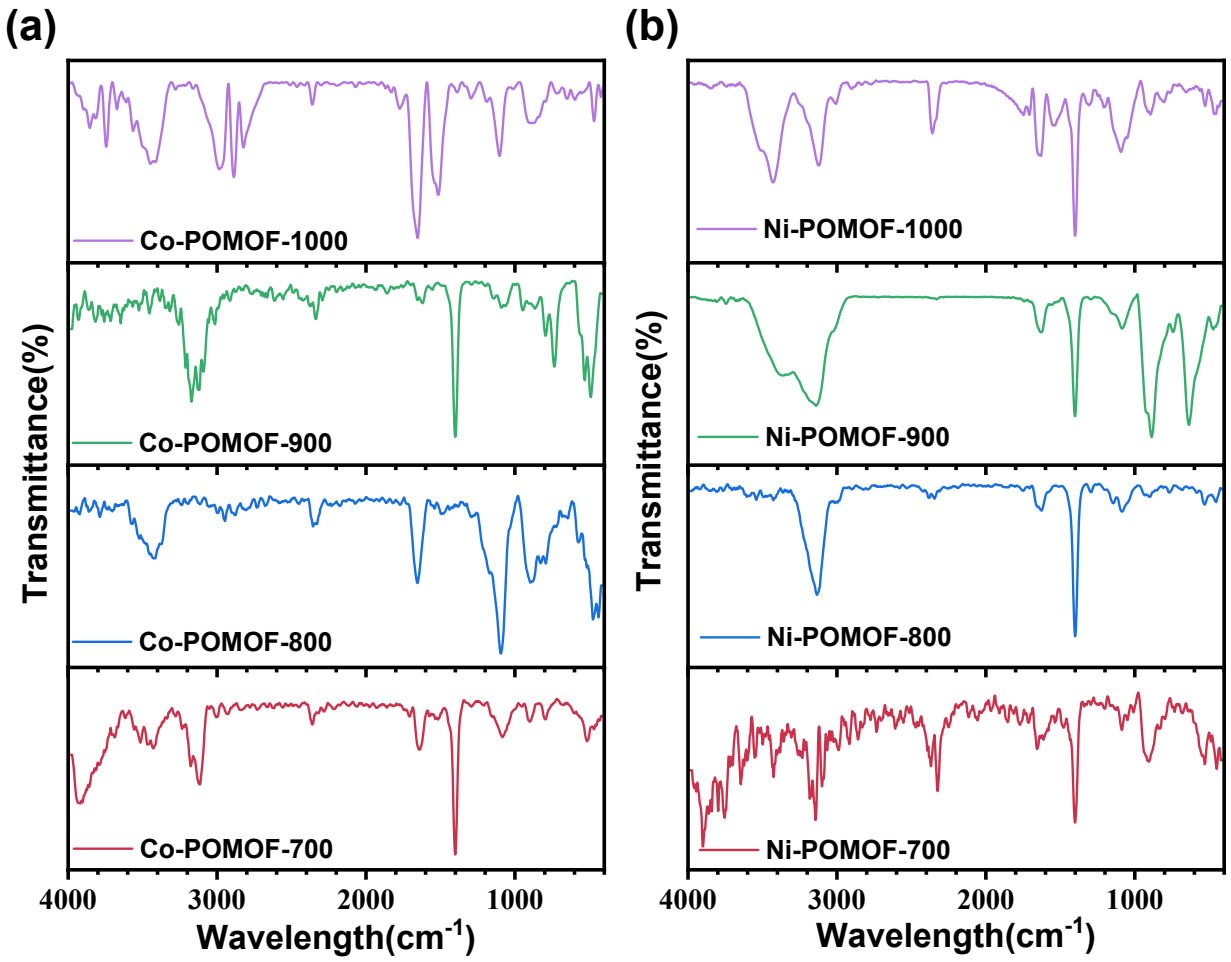

Figure S13: FT-IR spectra of (a) Co-POMOF-700, Co-POMOF-800, Co-POMOF-900 and Co-POMOF-1000, and (b) Ni-POMOF-700, Ni-POMOF-800, Ni-POMOF-900 and Ni-POMOF-1000.

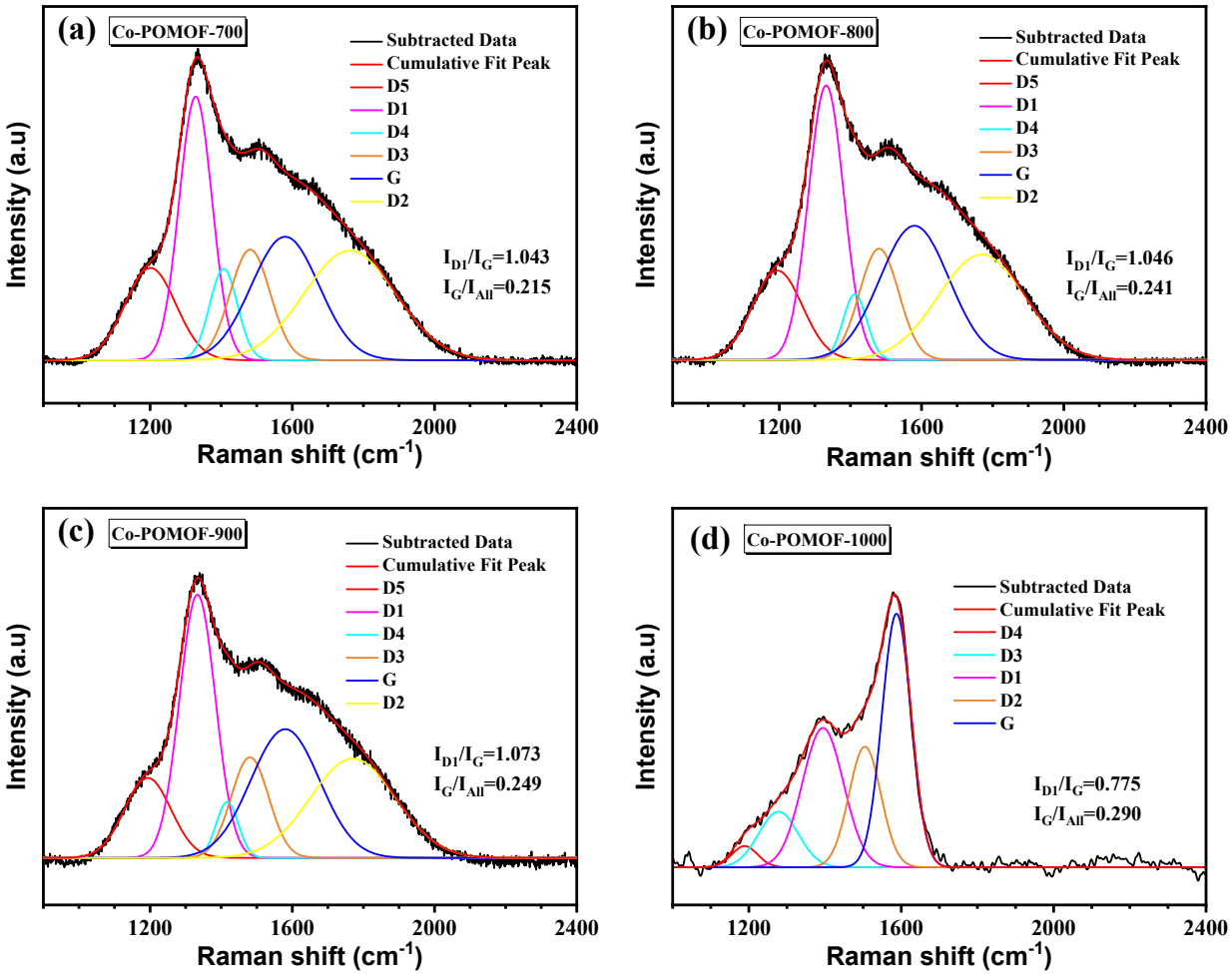

Figure S14: Raman spectra of (a) Co-POMOF-700, (b) Co-POMOF-800, (c) Co-POMOF-900 and (d) Co-POMOF-1000.

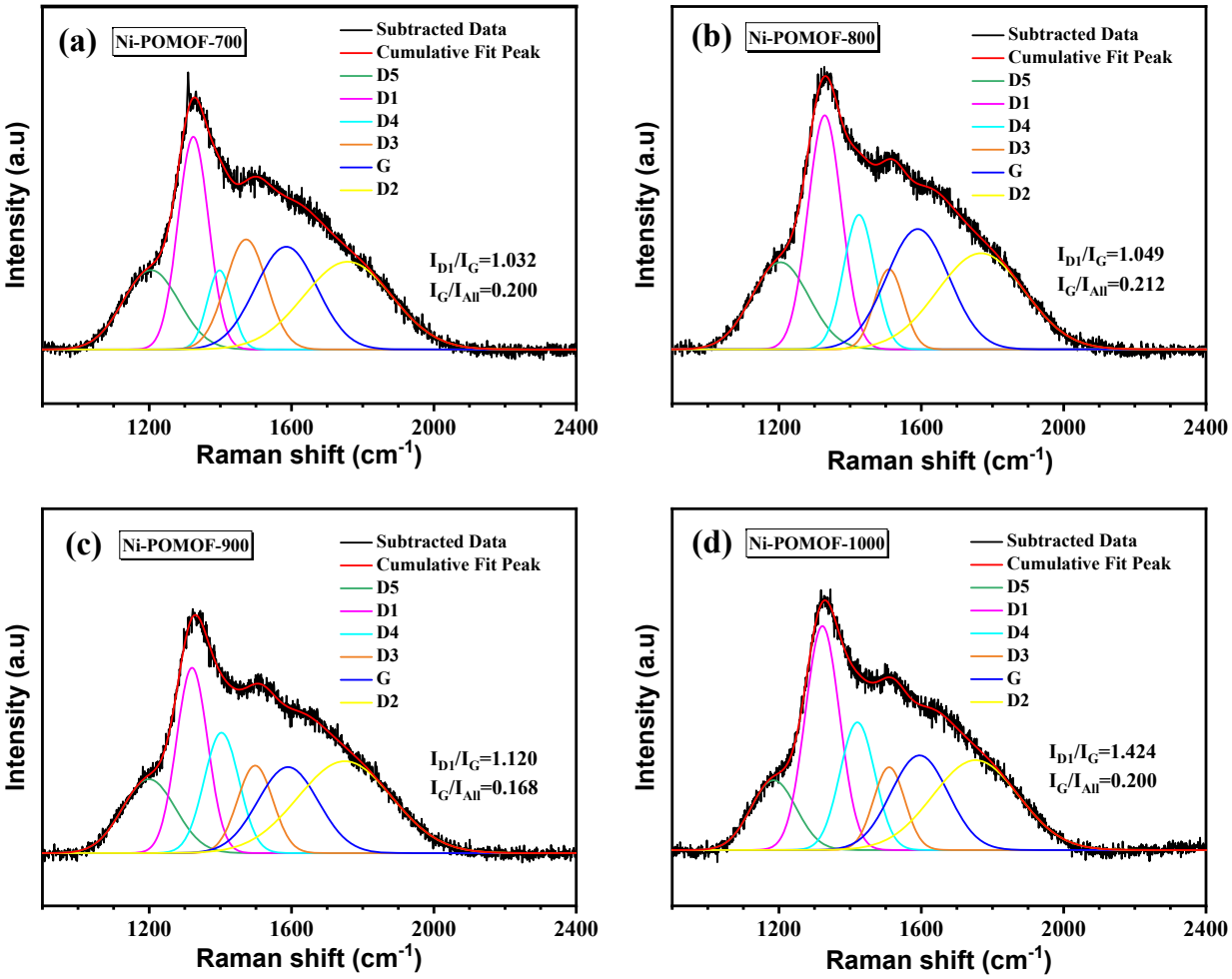

Figure S15: Raman spectra of (a) Ni-POMOF-700, (b) Ni-POMOF-800, (c) Ni-POMOF-900 and (d) Ni-POMOF-1000.

5. SEM, TEM and XPS

The catalysts prepared by Co-POMOF after calcination at 700 °C for 2 h showed a block structure with irregular shape and more nanoscale particles on the surface (Fig. S17(a,b)). In contrast, Ni-POMOF-900 had larger lumps and flatter surfaces, partly showing a distinct layer structure and fewer nanoscale particles on the surface (Fig. S17(c,d)).

Fig. S18(a – c) showed high resolution TEM images of Ni-POMOF-900. The lattice fringes with interlayer spacing of 0.245 nm was assigned to the (1 1 1 plane) of cubic Mo_2C structure (Fig. S18(b)), while the distances of 0.236 nm corresponded to the (0 0 2 plane) of hexagonal Mo_2C structure (Fig. S18(c)) [17]. In addition, four lattice fringes with lattice spacings of 0.221, 0.210, 0.242 and 0.212 nm were shown, corresponding to the (2 2 1) and (3 1 0) planes of Ni_2Mo_3N, and the (1 1 1) and (2 0 0) planes of Mo_2N, respectively (Fig. S18(b,c)). Fig. S18(d – i) showed the mapping images of Ni-POMOF-900. It can be seen that Ni, Mo, N, O and C elements were evenly distributed.

Through the analysis of OER performance of Co/Ni-POMOF-T series materials (T = 700/800/900/1000 °C), it was found that Co-POMOF-700 and Ni-POMOF-900 exhibited superior performance. As the calcination temperature of the Co/Ni-POMOF-T series materials increased, different inorganic compounds and phase transitions were observed. For example, Co_3Mo_3N in Co-POMOF-700 gradually transformed into Co_2Mo_3N with increasing temperature. This phase transition directly impacted the catalytic performance, possibly due to the lower catalytic activity of Co_2Mo_3N phase, while Co_3Mo_3N phase demonstrated better catalytic performance in OER. Similarly, in the Ni-POMOF-T series materials, as the temperature increased, the characteristic peak of Ni_2Mo_3N gradually intensified, and Ni_2Mo_3N was no longer dominant at 1000 °C. Through HR-TEM analysis, we further identified the lattice fringes of different phases, such as Ni_3Mo_3N, Ni_2Mo_3N, Mo_2N and Mo_2C, which provided further evidence for the presence of these phases and revealed the structural transformations occurring during the calcination process. These results indicated that the calcination temperature played a crucial role in the phase transition of the catalysts and their OER performance.

XPS experiments were carried out to determine the valence states of elements. The survey spectrum manifested the presence of Co, Mo, O, N and C elements in Co-POMOF (Fig. S19(a)). In the Co 2p spectrum of Co-POMOF (Fig. S20(a)), the peak positions of Co $2p_{3/2}$ and Co $2p_{1/2}$ were centered at 779.1 and 793.8 eV, corresponding to Co–N bonds, indicating that the cobalt atom was successfully coordinated with btap, further verified by the presence of N–Co coordination at 395.7 eV in the N 1s spectrum (Fig. S20(d)) [18]. The peaks at binding energies of 781.0 and 796.8 eV can be attributed to Co^{3+}, while the second spin–orbit doublet at binding energies of 782.8 and 798.5 eV can be attributed to Co^{2+} [19]. Fig. S20(b) showed the spectrum of Mo 3d, which can be deconvoluted into four peaks corresponding to Mo^{4+} (230.9 and 234.0 eV) and Mo^{6+} (232.6 and 235.7 eV). Fig. S20(d) showed the spectrum of N 1s, which can be decontaminated into four peaks at 395.7, 398.1, 400.0 and 401.4 eV, belonging to N–Co, pyridinic-N, nitrogen bond from btap ligand and residual NH_4^+, respectively. The elemental composition and chemical valences of Ni-POMOF were analyzed by XPS, which was composed of Ni, Mo, O, N and C elements (Fig. S19(b)). As

shown in Fig. S21(a), the XPS spectrum of Ni 2p, the peaks at 856.1 and 873.5 eV belonged to Ni^{2+}, while the peaks at 857.9 and 875.7 eV were assigned to Ni^{3+}. The Mo 3d spectrum revealed the existence of Mo^{5+} and Mo^{6+} in Ni-POMOF (Fig. S21(c)), where the Mo^{5+} and Mo^{6+} peaks located at 234.4 and 235.1 eV for Mo $2p_{3/2}$, and 231.3 and 231.9 eV for Mo $2p_{5/2}$, respectively. The N 1s peaks of Ni-POMOF (Fig. S21(g)) can also be deconvoluted into four peaks as N–Ni (396.8 eV), pyridinic-N (398.1 eV), nitrogen bond from btap ligand (399.1 eV) and residual NH_4^+ (400.3 eV) [18]. Before OER, Ni 2p XPS spectrum of Ni-POMOF-900 showed peaks at 856.8/858.3 eV of Ni $2p_{3/2}$ and 874.4/876.2 eV of Ni $2p_{1/2}$, corresponding to Ni^{2+} and Ni^{3+}, respectively (Fig. S21(b)). After OER, 856.5/857.8 eV of Ni $2P_{3/2}$ and 874.3/874.5 eV of Ni $2p_{1/2}$ were ascribed to $Ni(OH)_2$ and NiOOH [20]. Before OER, O 1s spectrum of Ni-POMOF-900 showed peaks located at 531.2 and 532.5 eV belonging to the lattice oxygen and adsorbed water molecule (Fig. S21(f)) [21]. After OER, H_2O and oxide ions (O_2^-) from NiOOH peaks appeared at 532.3 and 533.5 eV [20, 21], respectively. The binding energies of 227.4/230.1/233.3 eV of Mo $3d_{5/2}$ and 230.4/233.3/236.4 eV of Mo $3d_{3/2}$ were assigned to Mo–N, Mo^{4+} and Mo^{5+}, which were found mainly in Ni_2Mo_3N phase (Fig. S21(d)). Nevertheless, Mo–N peaks completely disappeared after OER. Before OER, the binding energies of 396.1/398.8 eV of N 1s correspond to N–Mo/Ni and pyridinic-N [18]. After OER, N–Mo/Ni peaks completely disappeared.

Table S9: XPS binding energies for the materials

Sample	**M[a] $2p_{3/2}$ (eV)[b]**	**Mo 3d $2p_{5/2}$ (eV)**	**O 1s (eV)**	**N 1s (eV)**
Co-POMOF	779.1/781.0/782.8	230.9/232.6	530.5/531.2/532.8	395.7/398.1/400.0/401.4
Co-POMOF after OER	780.4/781.2	231.3/232.4	530.3/531.5/532.9	398.0/400.4/403.3
Co-POMOF-700	778.3/780.2/781.5	228.1/229.5/231.9	530.0/532.0	396.9/394.1/398.1
Co-POMOF-700 after OER	780.5/782.8	230.5/232.3	529.9/531.3/532.0	398.5/400.4/403.9
Ni-POMOF	856.1/857.9	231.3/231.9	529.1/530.0/531.6	396.8/398.1/399.1/400.3
Ni-POMOF after OER	854.4/855.6	229.2/232.5	531.3/531.8	395.7/399.4/400.6
Ni-POMOF-900	856.8/858.3	227.4/230.1/233.3	531.2/532.5	396.1/398.8
Ni-POMOF-900 after OER	856.5/857.8	232.9/233.9	532.3/533.5	398.2/401.1

[a] M = Co or Ni.

[b] All peaks were referenced to C ls at 284.8 eV.

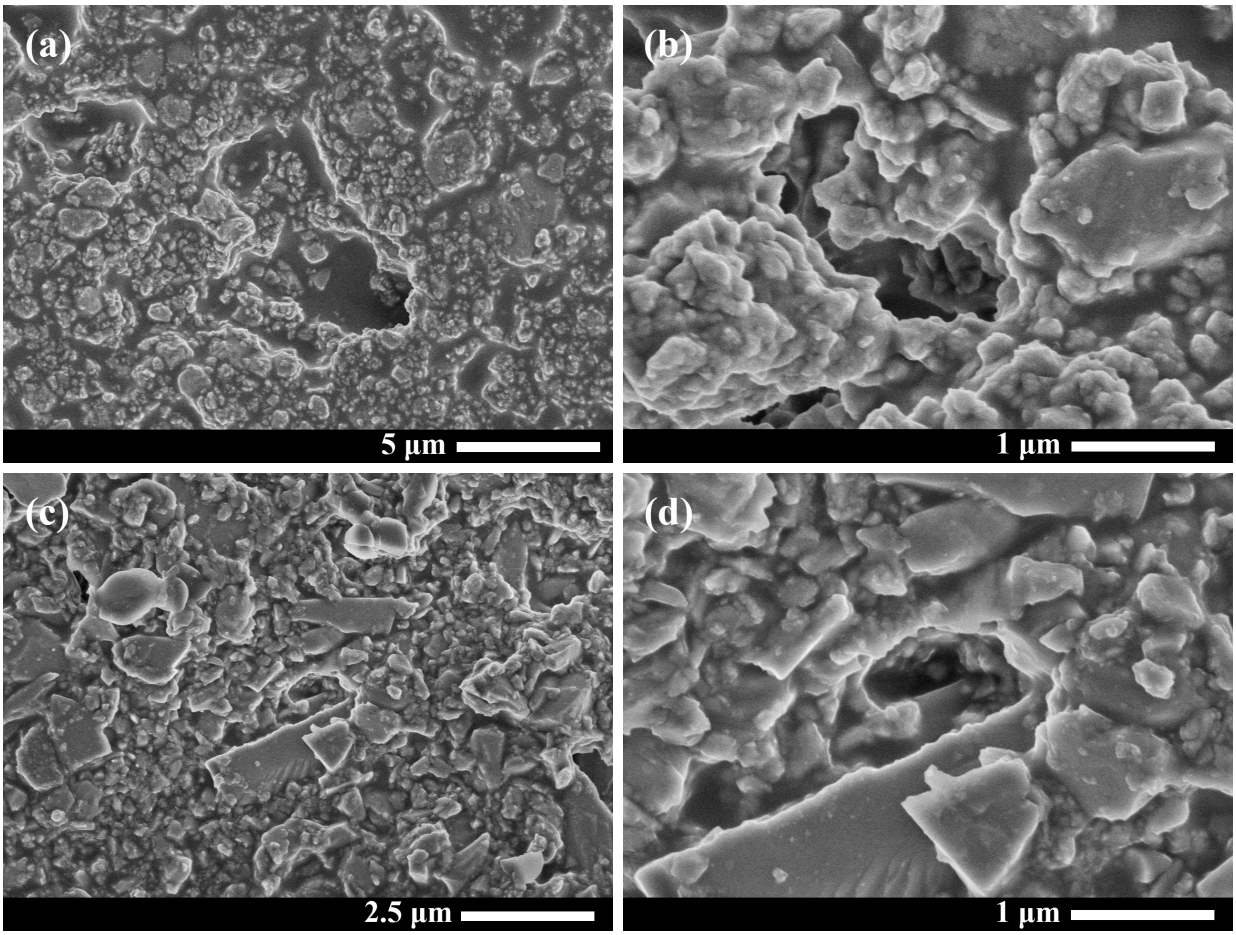

Figure S16: SEM images of (a)(b) Co-POMOF and (c)(d) Ni-POMOF.

Table S10: Atomic ratios of surface species determined by the XPS survey spectra and the relative ratios

Sample	**O (at.%)**	**N (at.%)**	**Mo (at.%)**	**M[a] (at.%)**	**N/M[a]**	**Mo/M[a]**
Co-POMOF	30.81	32.02	16.16	6.13	5.22	2.64
Co-POMOF after OER	8.16	2.27	0.61	3.74	0.61	0.16
Co-POMOF-700	19.84	28.11	21.16	6.37	4.41	3.32
Co-POMOF-700 after OER	13.52	0.78	0.29	1.75	0.45	0.17
Ni-POMOF	17.89	39.79	13.67	3.12	12.75	4.38
Ni-POMOF after OER	10.02	0.75	0.12	2.63	0.29	0.05
Ni-POMOF-900	19.40	27.83	28.27	6.03	4.62	4.69
Ni-POMOF-900 after OER	16.76	0.50	0.13	4.19	0.20	0.03

[a] M = Co or Ni.

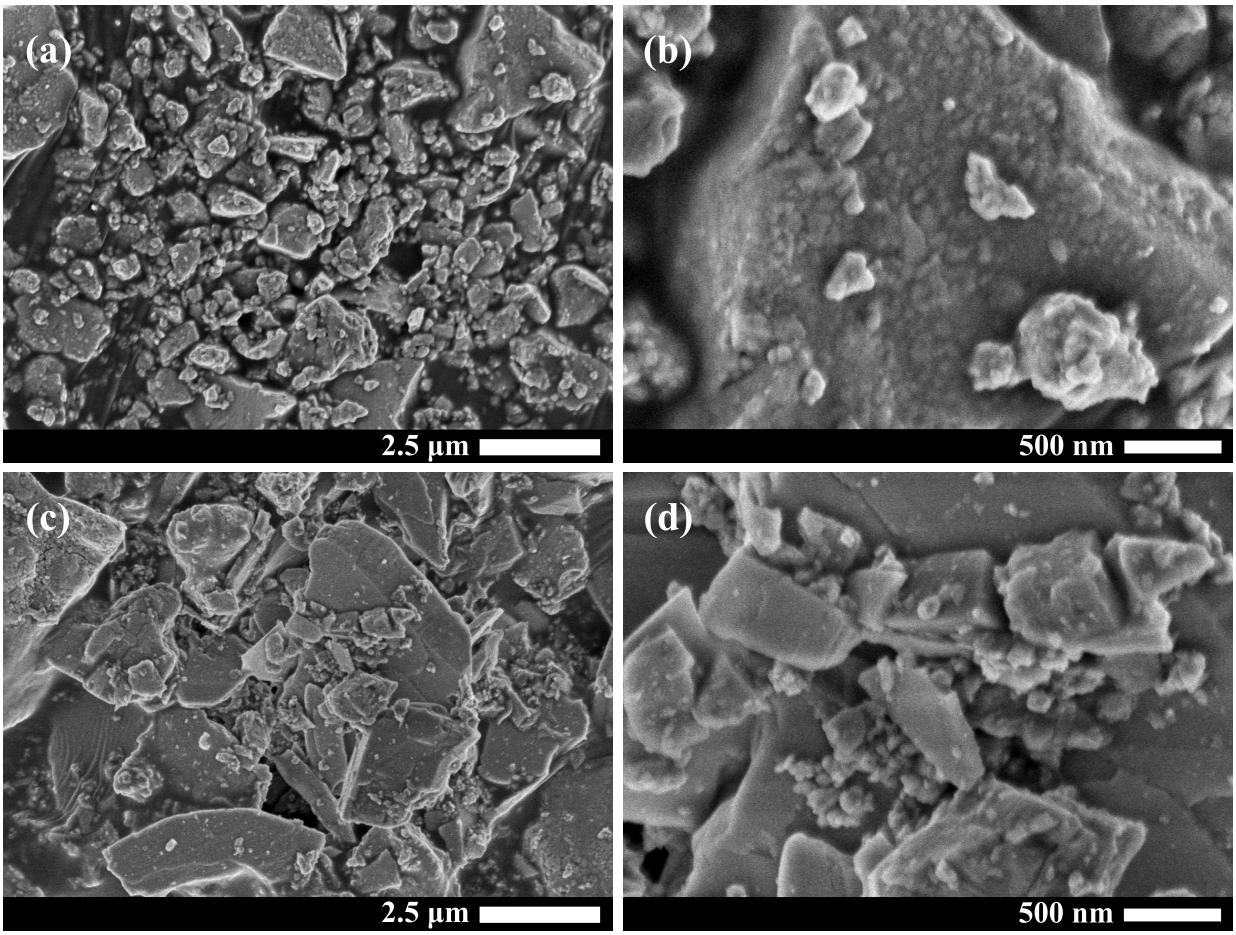

Figure S17: SEM images of (a)(b) Co-POMOF-700 and (c)(d) Ni-POMOF-900.

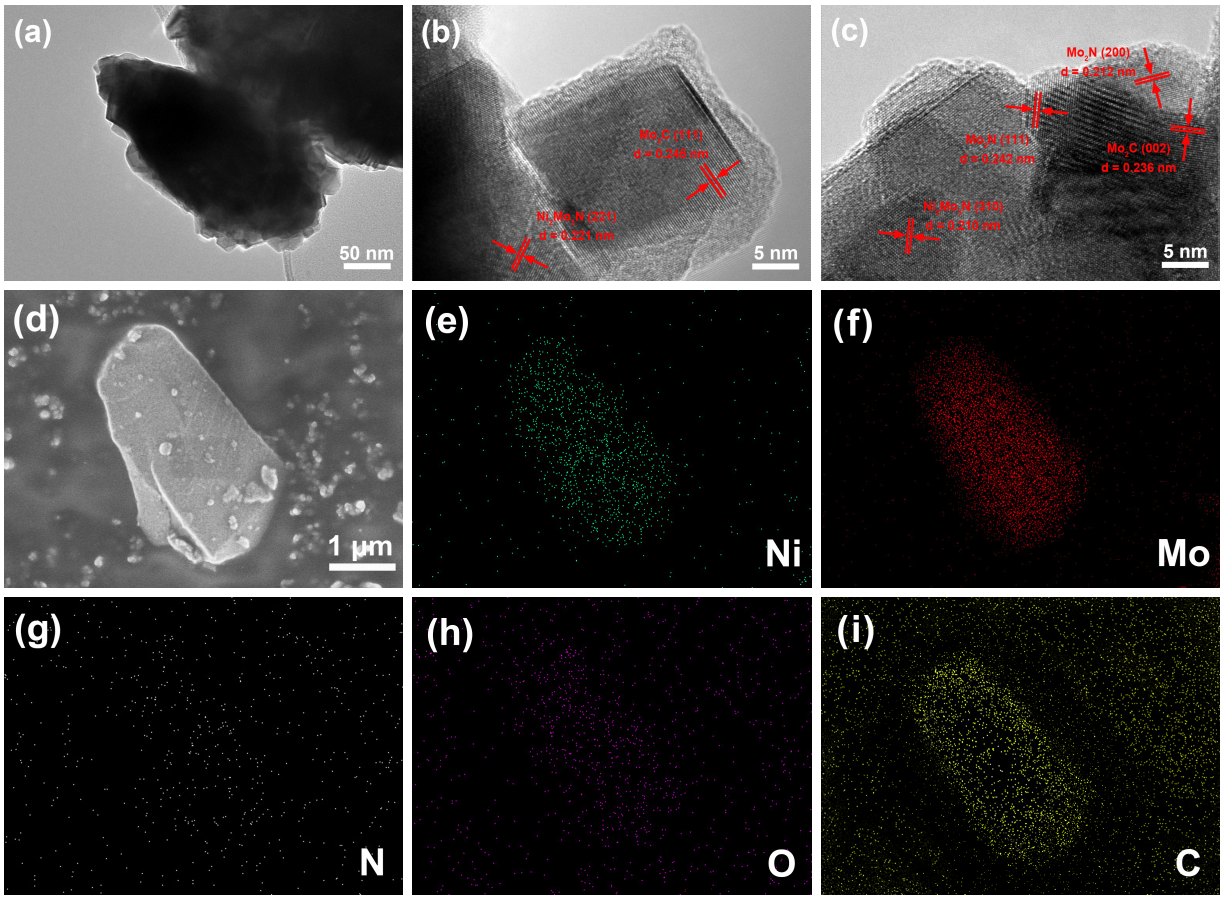

Figure S18: (a) TEM and (b,c) HR-TEM images of Ni-POMOF-900. (d – i) EDX mapping images of Ni-POMOF-900.

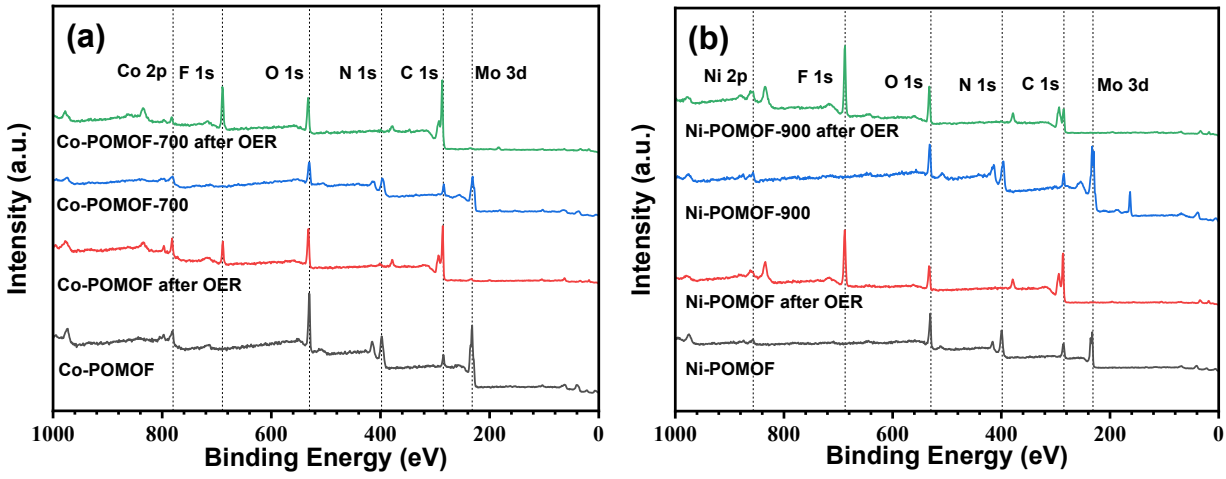

Figure S19: (a) XPS spectra of Co-POMOF before and after OER, and Co-POMOF-700 before and after OER. (b) XPS spectra of Ni-POMOF before and after OER, and Ni-POMOF-900 before and after OER.

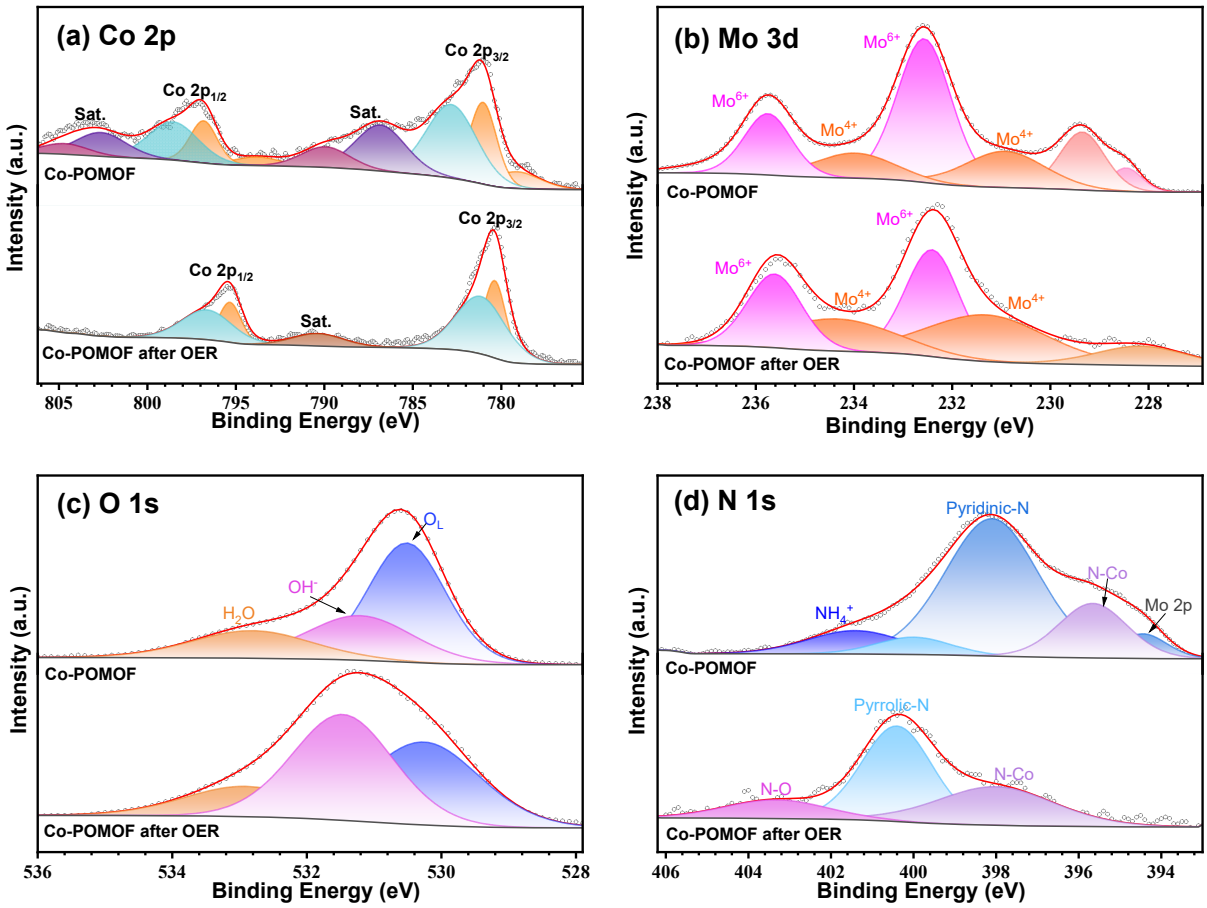

Figure S20: (a) Co 2p XPS spectra of Co-POMOF before and after OER. (b) Mo 3d XPS spectra of Co-POMOF before and after OER. (c) O 1s XPS spectra of Co-POMOF before and after OER. (d) N 1s XPS spectra of Co-POMOF before and after OER.

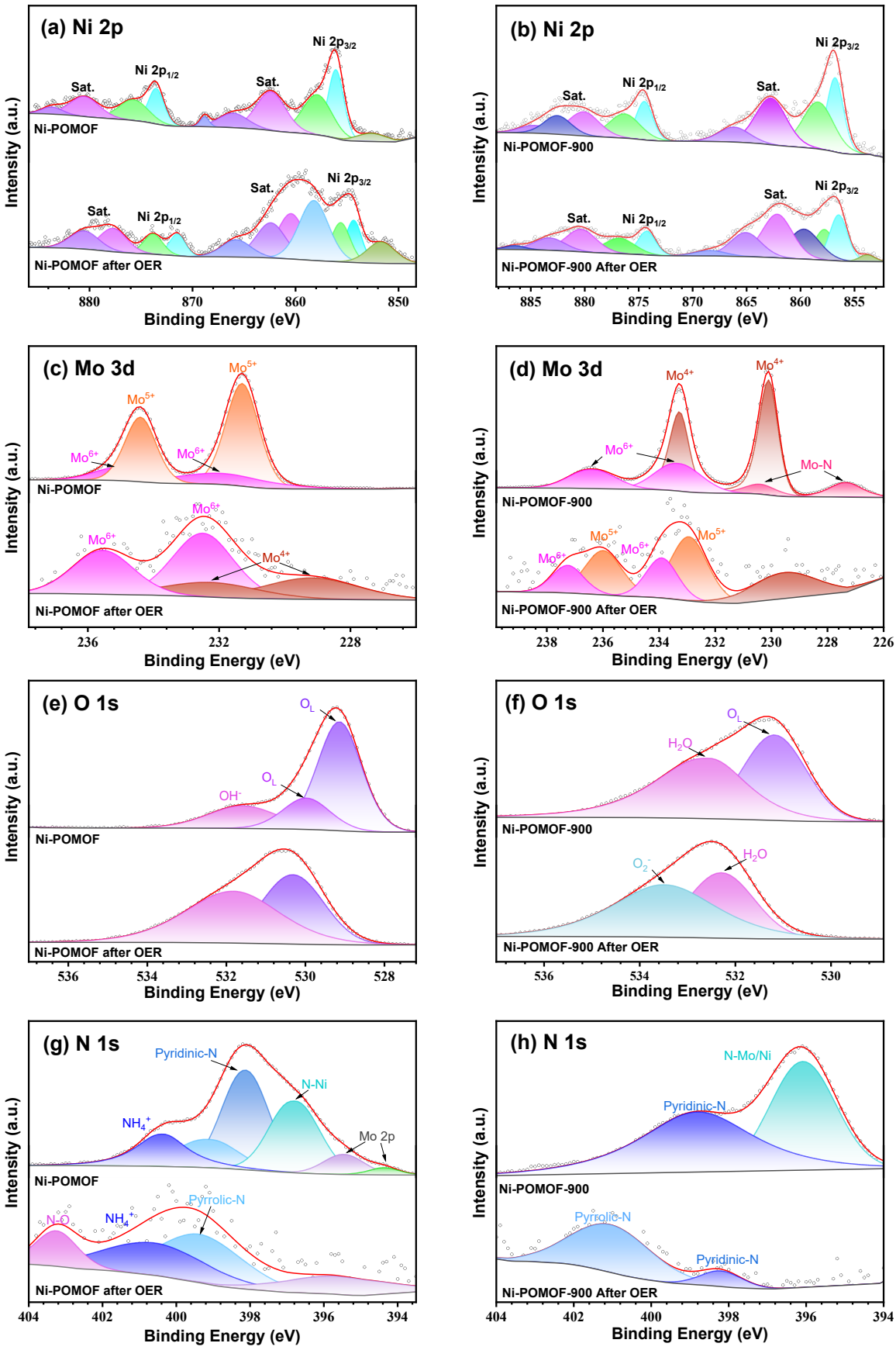

Figure S21: Ni 2p XPS spectra of (a) Ni-POMOF, and (b) Ni-POMOF-900 before and after OER. Mo 3d XPS spectra of (c) Ni-POMOF, and (d) Ni-POMOF-900 before and after OER. O 1s XPS spectra of (e) Ni-POMOF, and (f) Ni-POMOF-900 before and after OER. N 1s XPS spectra of (g) Ni-POMOF, and (h) Ni-POMOF-900 before and after OER.

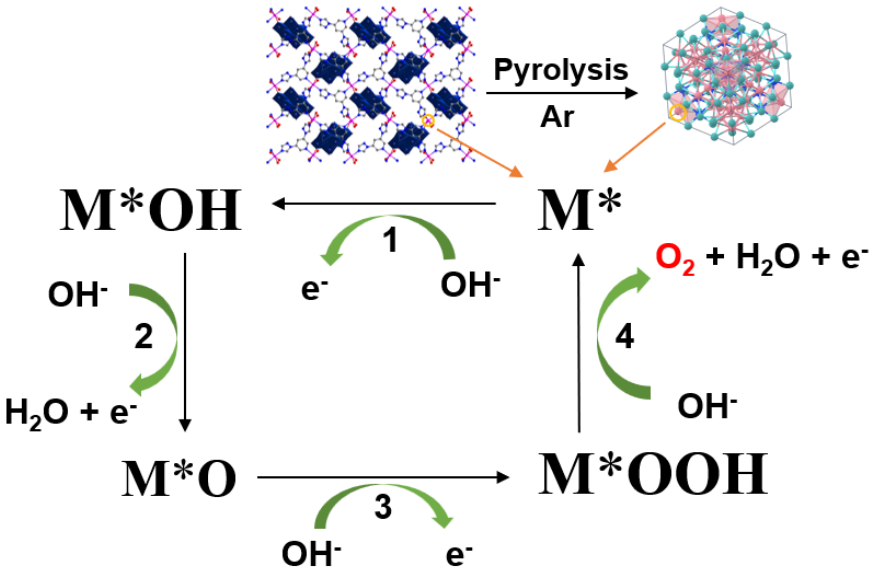

Figure S22: OER pathway.

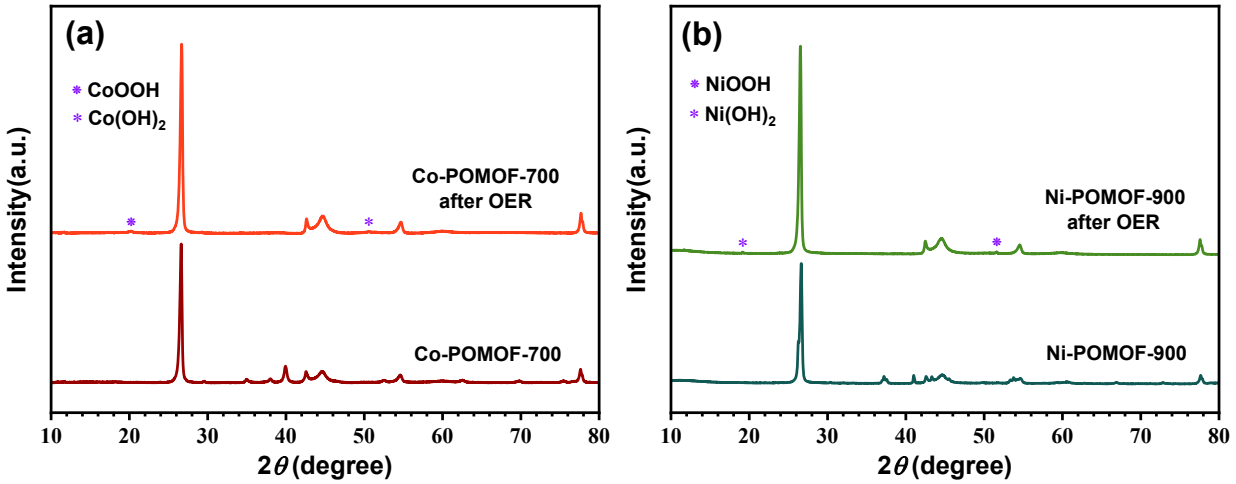

Figure S23: (a) PXRD patterns of Co-POMOF-700/GE before and after OER. (b) PXRD patterns of Ni-POMOF-900/GE before and after OER.

6. Electrochemical Properties of Co/Ni-POMOF and Co/Ni-POMOF-T

6.1. Preparation of Working Electrodes

Modified graphite electrodes (GE) were used as working electrodes [22]. The working electrodes were prepared according to the following process. After being polished with 0.3 and 0.05 μm Al_2O_3 particles, the graphite substrate electrode (1 cm × 1 cm × 0.5 cm) was cleaned with ultrapure H_2O. POMOF or its thermal derivatives were mixed with polyvinylidene fluoride (PVDF) and carbon black by adequate grinding in an appropriate mass ratio at 1 ml of *N* -methyl-2-pyrrolidone (NMP) and ink suspension was obtained. The obtained slurry was homogenized by ultrasonication, and 100 μL of the slurry was dropped onto the graphite electrode to form a thin film, and then dried under an infrared lamp. The other surfaces of the graphite electrode were covered with a thin polytetrafluoroethylene (PTFE) film and the electrode surface area, $A = 1$ cm × 1 cm. All of the working electrodes were kept in a desiccator prior to electrochemical measurements.

6.2. Electrochemical Measurements

All electrochemical measurements were performed in an aqueous solution of 1 M KOH (pH ≈ 14) at room temperature. The three-electrode system was connected to an electrochemical workstation (CHI 660E, CH Instruments), where the reference electrode was a saturated calomel electrode (SCE, Hg/Hg_2Cl_2) and the counter electrode was a platinum wire. Linear sweep voltammetry (LSV) was measured at a scan rate of 5 mV s^{-1} with 85 % *iR* compensation [23]. Working potentials were converted with respect to the reversible hydrogen electrode (RHE) according to the following equation:

$$E_{\mathrm{RHE}} = E_{\mathrm{SCE}} + 0.059 \times \mathrm{pH} + 0.2415\ (\mathrm{V}) \tag{1}$$

For the LSV curve of oxygen eVolution reaction (OER), the overpotential (η) of each electrode material was calculated according to the following equation [24]:

$$\eta = E_{\mathrm{RHE}} - 1.23\ (\mathrm{V}) \tag{2}$$

The Tafel slope was calculated according to the following equation [25–28]:

$$\eta = b \log |j| + a \tag{3}$$

with η the overpotential in mV, b the Tafel slope in mV dec^{-1}, j the current density in mA cm^{-2}, and a the exchange current density.

Double layer capacitance (C_{dl}) was calculated in the non-Faradaic potential region by cyclic voltammetry (CV) curves at different scanning rates [29].

The electrochemical impedance spectroscopy (EIS) was performed in the frequency region of 10^5 to 10^{-2} Hz with an amplitude of 5 mV. Electrocatalytic stability was assessed by polarization curves (LSV) measured with the 1000 or 2000 CV cycle in 1 M KOH solution, and $i - t$ curves were obtained by chronoamperometry at constant operating voltage for 12 or 24 hours.

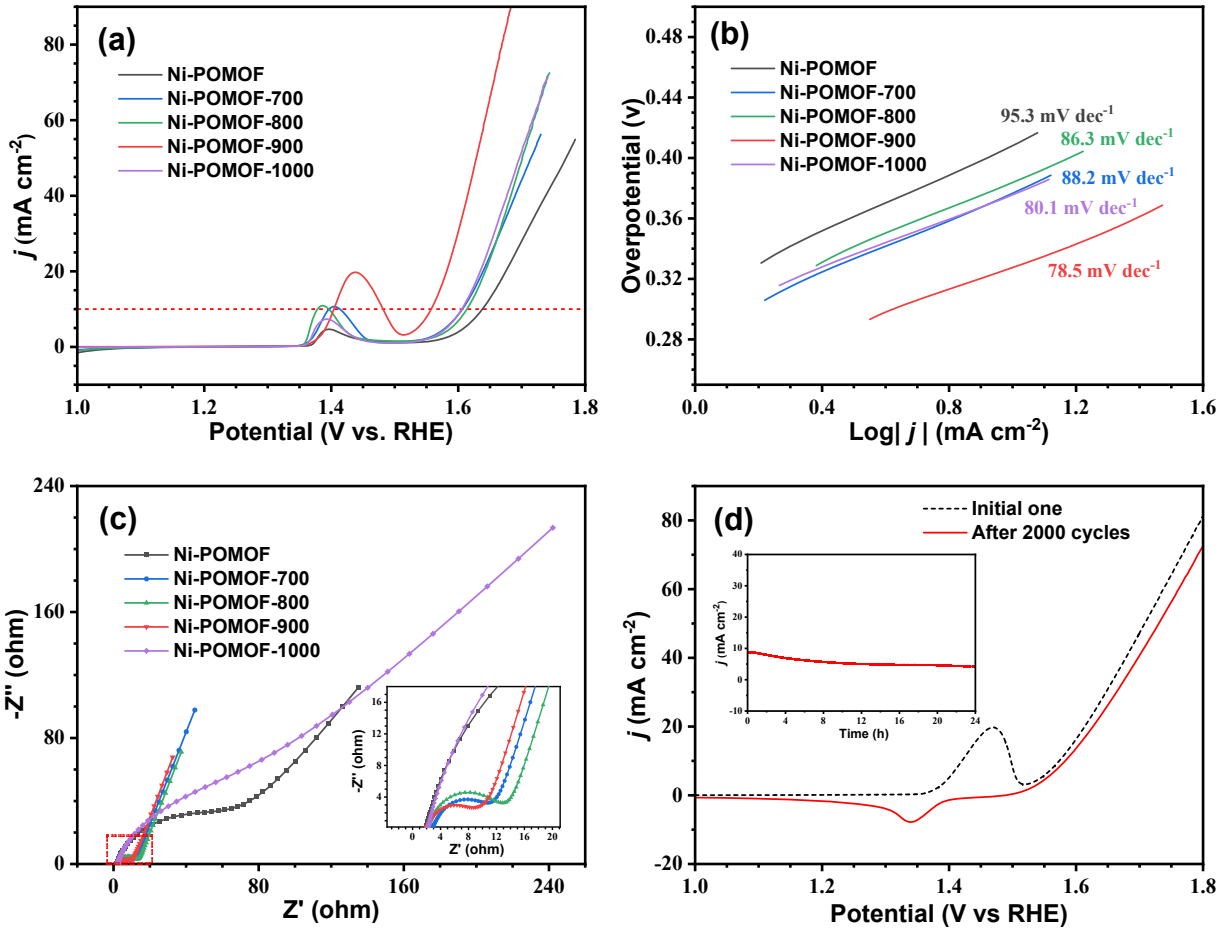

Figure S24: (a) LSV curves with the potential range of 1.0 to 1.8 V (*vs.* RHE) in 1 M KOH for OER. (b) Tafel plots from the LSV curves. (c) EIS curves. (d) LSV curves of Ni-POMOF-900 before and after 2000 CV cycles (inset: chronoamperometric measurement at 10 mA cm^{-2} for Ni-POMOF-900 in 24 h.

By fitting Δj ($\Delta j = |j_{pa} - j_{pc}|$) to the scanning rate, the C_{dl} value of Co-POMOF-700 (6.2 mF cm^{-2}) was calculated to be slightly higher than that of Co-POMOF (4.2 mF cm^{-2}) (Fig. S25(a,b)), and the C_{dl} value of Ni-POMOF-900 (5.9 mF cm^{-2}) was also slightly higher than that of Ni-POMOF (2.0 mF cm^{-2}) (Fig. S25(c,d)). The improved OER performance of Co-POMOF-700 and Ni-POMOF-900 can be attributed in part to their better intrinsic activity, with Co-POMOF-700 and Ni-POMOF-900 having a greater specific surface area, which can expose more active sites.

The electrocatalytic activities of Co-POMOF-T with a mass loading of 1.0 mg cm^{-2} in 1 M KOH toward OER were studied. As widely accepted, the Co^{2+} species in Co-based electrocatalysts generally experienced obvious oxidation processes and transformed into high-oxidation cobalt species, which was critical to their electrocatalytic performances. This CV process can be viewed as a precatalytic treatment of $Co^{2+} \rightarrow Co^{3+} \rightarrow Co^{4+}$ activation in alkaline medium, and indicated that the active sites of OER mainly resulted from surface redox reactions.

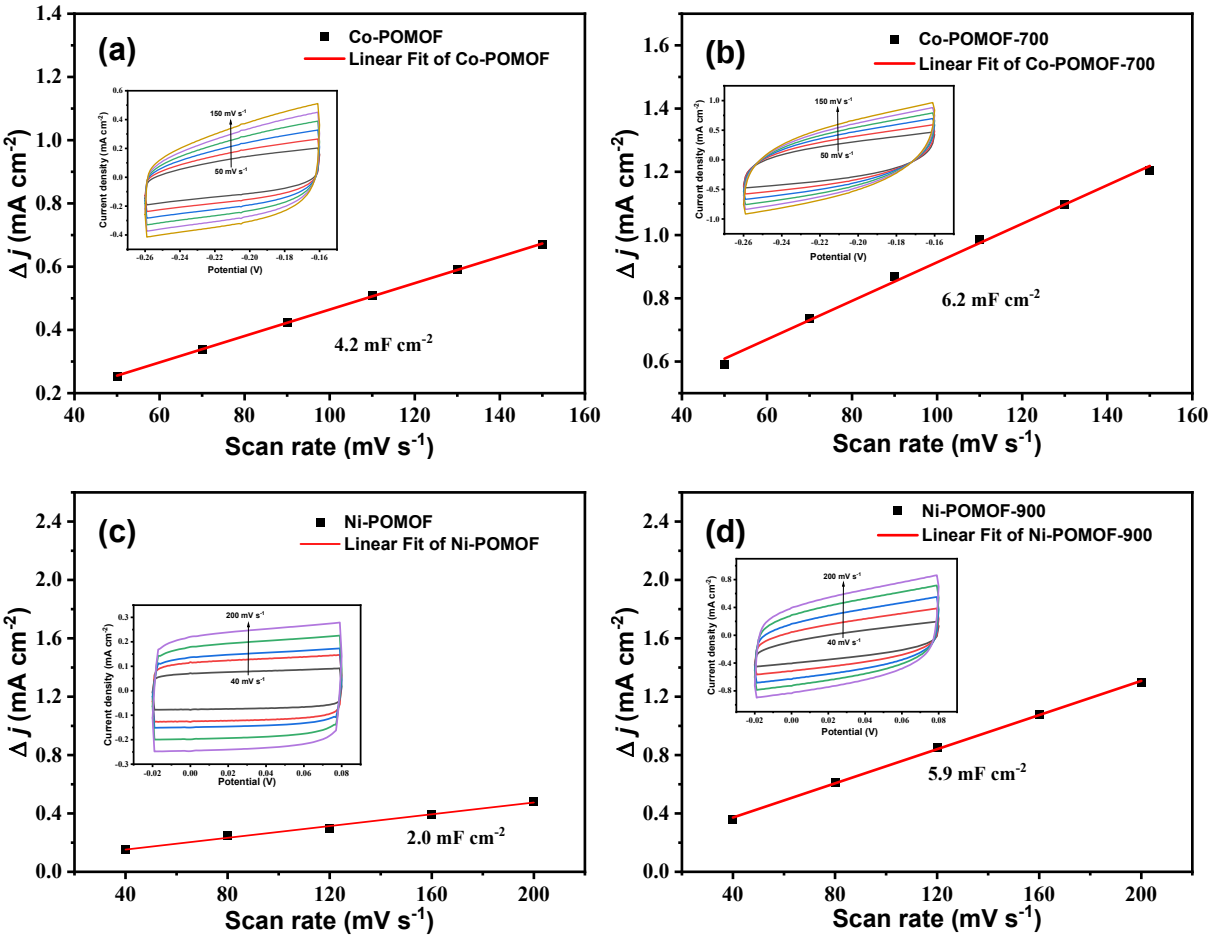

Figure S25: Double-layer capacitance (C_{dl}) from the CV curves (Insert: CV curves) for (a) Co-POMOF, (b) Co-POMOF-700, (c) Ni-POMOF and (d) Ni-POMOF-900.

Fig. S26(a,c,e,g,i) showed the CV plots of various electrodes at a scan rate from 10 to 190 mV s^{-1} with a step of 20 mV s^{-1}. A pair of redox peaks appeared at around 1.0 V and 1.4 V *vs.* RHE can be clearly seen in eVery scan cycle of these curves, which might originate from the change between Co ions of different valence states ($Co^{2+} \rightarrow Co^{3+}$) similar to the previous reports of many Co-based materials [30]. Different from the Ni materials with only a pair of redox peaks, another pair of redox peaks of $Co^{3+} \rightarrow Co^{4+}$ appeared at about 1.3 V and 1.6 V *vs.* RHE. The results of the anodic peak potential (E_{pa}), the cathodic peak potential (E_{pc}), the half-wave potential ($E_{1/2} = (E_{pa} + E_{pc})/2$), and the potential peak separation ($\Delta E_p = |E_{pa} - E_{pc}|$) for the pair of waves were reported in Table S11. When the scan rate increased from 10 to 190 mV s^{-1}, ΔE_p increased slightly. The cathodic peak current densities (j_{pc}) and the anode peak current densities (j_{pa}) of the $Co^{2+} \rightarrow Co^{3+}$ redox peaks were linear with the scan rates, as shown in Fig. S26(b,d,f,h,j), indicating that the process belonged to the surface controlled electrode process. For an ideal electrode, the peak potential does not change with scan rate [31]. In fact, the reversibility of an electrode reaction is related to the scanning rate. At low scan rates, the electrode reaction

shows reversible characteristics. While at high scan rates, the charge transfer reaction rate and mass transfer process no longer follow the Nernst equation, and the electrode reaction changes from reversible to irreversible [32]. The absolute values of j_{pc} and j_{pa} were roughly equal at the low sweep rates, which meant that the ratio of the absolute value of j_{pc} and j_{pa} was close to 1. The value of ΔE_p approached 59/n mV, but $E_{1/2}$ and ΔE_p increased with increasing scan rate [32]. The electrode reaction was quasi-reversible [33]. $E_{1/2}$ and ΔE_p data for the $Co^{2+} \rightarrow Co^{3+}$ redox peaks were tabulated in Table S11.

Ni-POMOF-T was also configured as anode materials (mass loading 1.0 mg cm^{-2}) in 1 M KOH for OER performance. Usually, a couple of redox peaks can be observed in those typical cyclic voltammetry (CV) curves of Ni-based materials, and the pair of sharp peaks belonged to the redox electric pair peaks $Ni^{2+} \rightarrow Ni^{3+}$ [34]. Fig. S27(a,c,e,g,i) displayed the CV curves of the four Ni-POMOF-T at different scan rates. The results of E_{pa}, E_{pc}, $E_{1/2}$ and ΔE_p were reported in Table S12. It can be seen that j_{pc} and j_{pa} depended linearly on the square roots of the sweep rates (Fig. S27(b,d,f,h,j)), indicating that the diffusion of the electrolyte was dominant in the redox process for the Ni-POMOF-T.

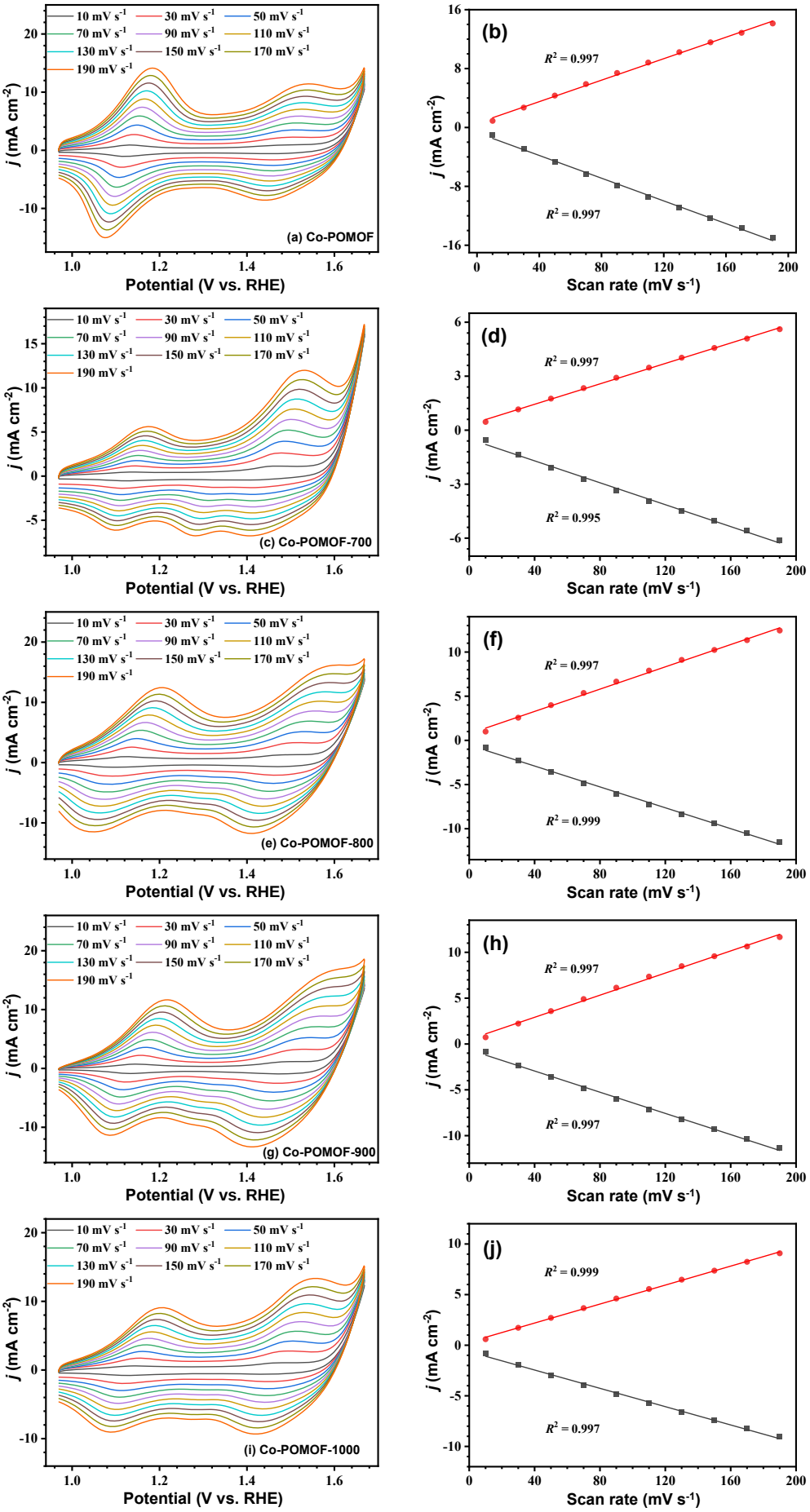

Figure S26: CV curves of (a) Co-POMOF, (c) Co-POMOF-700, (e) Co-POMOF-800, (g) Co-POMOF-900 and (i) Co-POMOF-1000 at different scan rates (10, 30, 50, 70, 90, 110, 130, 150, 170 and 190 mv s^{-1} with 0.97 to 1.67 V (*vs.* RHE). The linear relationship between the anode (red) and cathode (black) CV current densities with different scan rates of (b) Co-POMOF, (d) Co-POMOF-700, (f) Co-POMOF-800, (h) Co-POMOF-900 and (j) Co-POMOF-1000.

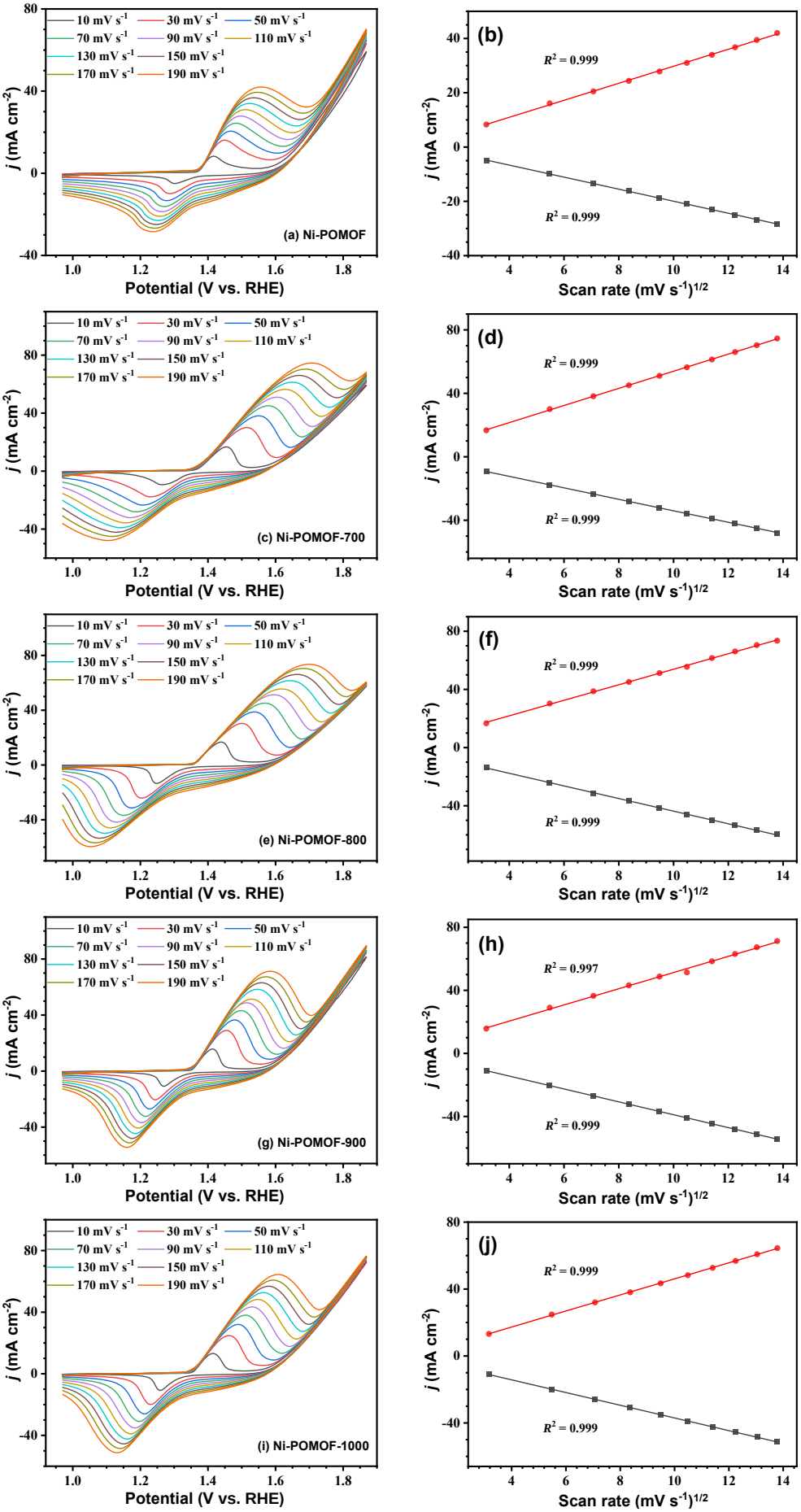

Figure S27: CV curves of (a) Ni-POMOF, (c) Ni-POMOF-700, (e) Ni-POMOF-800, (g) Ni-POMOF-900 and (i) Ni-POMOF-1000 at different scan rates (10, 30, 50, 70, 90, 110, 130, 150, 170 and 190 mv s^{-1} with 0.97 to 1.87 V (*vs.* RHE). The linear relationship between the anode (red) and cathode (black) CV current densities with different half of the square of the scan rates of (b) Ni-POMOF, (d) Ni-POMOF-700, (f) Ni-POMOF-800, (h) Ni-POMOF-900 and (j) Ni-POMOF-1000.

Table S11: $E_{1/2}$ and ΔE_{p} data of the Co-POMOFs materials

Sample	**Scan rate**	$E_{\mathbf{pc}}$	$E_{\mathbf{pa}}$	$E_{1/2}$	$\Delta E_{\mathbf{p}}$
	(mV s^{-1})	**(V)**	**(V)**	**(V)**	**(mV)**
Co-POMOF	10	1.1199	1.1339	1.1269	14
	30	1.1129	1.1399	1.1264	27
	50	1.1069	1.1489	1.1279	42
	70	1.1019	1.1529	1.1274	51
	90	1.0969	1.1609	1.1289	64
	110	1.0929	1.1659	1.1294	73
	130	1.0869	1.1719	1.1294	85
	150	1.0829	1.1739	1.1284	91
	170	1.0779	1.1779	1.1279	100
	190	1.0749	1.1829	1.1289	108
Co-POMOF-700	10	1.1209	1.1369	1.1289	16
	30	1.1159	1.1449	1.1304	29
	50	1.1139	1.1479	1.1309	34
	70	1.1099	1.1529	1.1314	43
	90	1.1079	1.1559	1.1319	48
	110	1.1049	1.1589	1.1319	54
	130	1.1059	1.1639	1.1349	58
	150	1.1029	1.1689	1.1359	66
	170	1.1009	1.1719	1.1364	71
	190	1.0999	1.1749	1.1374	75
Co-POMOF-800	10	1.0889	1.1229	1.1059	34
	30	1.0919	1.1369	1.1144	45
	50	1.0869	1.1479	1.1174	61
	70	1.0799	1.1589	1.1194	79
	90	1.0689	1.1669	1.1179	98
	110	1.0689	1.1769	1.1229	108
	130	1.0619	1.1849	1.1234	123
	150	1.0589	1.1899	1.1244	131
	170	1.0489	1.1969	1.1229	148
	190	1.0429	1.2029	1.1229	160
Co-POMOF-900	10	1.0889	1.1229	1.1059	34
	30	1.0919	1.1369	1.1144	45
	50	1.0869	1.1479	1.1174	61
	70	1.0799	1.1589	1.1194	79
	90	1.0689	1.1669	1.1179	98
	110	1.0689	1.1769	1.1229	108
	130	1.0619	1.1849	1.1234	123
	150	1.0589	1.1899	1.1244	131

Continued on next page

Table S11 – continued from previous page

Sample	Scan rate	E_{pc}	E_{pa}	$E_{1/2}$	ΔE_p
	(mV s^{-1})	(V)	(V)	(V)	(mV)
	170	1.0489	1.1969	1.1229	148
	190	1.0429	1.2029	1.1229	160
Co-POMOF-1000	10	1.1199	1.1449	1.1324	25
	30	1.1189	1.1529	1.1359	34
	50	1.1129	1.1609	1.1369	48
	70	1.1089	1.1689	1.1389	60
	90	1.1059	1.1749	1.1404	69
	110	1.0999	1.1819	1.1409	82
	130	1.0969	1.1879	1.1424	91
	150	1.0939	1.1929	1.1434	99
	170	1.0929	1.1989	1.1459	106
	190	1.0899	1.2039	1.1469	114

Table S12: $E_{1/2}$ and ΔE_{p} data of the Ni-POMOFs materials

Sample	**Scan rate**	$E_{\mathbf{pc}}$	$E_{\mathbf{pa}}$	$E_{1/2}$	$\Delta E_{\mathbf{p}}$
	(mV s^{-1})	**(V)**	**(V)**	**(V)**	**(mV)**
Ni-POMOF	10	1.3019	1.4169	1.3594	115
	30	1.2879	1.4499	1.3689	162
	50	1.2779	1.4669	1.3724	189
	70	1.2709	1.4819	1.3764	211
	90	1.2629	1.4959	1.3794	233
	110	1.2579	1.5109	1.3844	253
	130	1.2509	1.5219	1.3864	271
	150	1.2469	1.5329	1.3899	286
	170	1.2409	1.5469	1.3939	306
	190	1.2369	1.5569	1.3969	320
Ni-POMOF-700	10	1.2639	1.4539	1.3589	190
	30	1.2299	1.5149	1.3724	285
	50	1.2049	1.5489	1.3769	344
	70	1.1859	1.5779	1.3819	392
	90	1.1689	1.6039	1.3864	435
	110	1.1539	1.6269	1.3904	473
	130	1.1399	1.6479	1.3939	508
	150	1.1269	1.6699	1.3984	543
	170	1.1139	1.6869	1.4004	573
	190	1.1009	1.7059	1.4034	605
Ni-POMOF-800	10	1.2479	1.4389	1.3434	191
	30	1.2039	1.5009	1.3524	297
	50	1.1739	1.5369	1.3554	363
	70	1.1489	1.5669	1.3579	418
	90	1.1299	1.5949	1.3624	465
	110	1.1099	1.6179	1.3639	508
	130	1.0929	1.6419	1.3674	549
	150	1.0789	1.6629	1.3709	584
	170	1.0649	1.6829	1.3739	618
	190	1.0509	1.6989	1.3749	648
Ni-POMOF-900	10	1.2689	1.4129	1.3409	144
	30	1.2439	1.4539	1.3489	210
	50	1.2269	1.4789	1.3529	252
	70	1.2149	1.4979	1.3564	283
	90	1.2029	1.5129	1.3579	310
	110	1.1929	1.5279	1.3604	335
	130	1.1849	1.5449	1.3649	360
	150	1.1759	1.5579	1.3669	382

Continued on next page

Table S12 – continued from previous page

Sample	Scan rate ($mV\ s^{-1}$)	E_{pc} (V)	E_{pa} (V)	$E_{1/2}$ (V)	ΔE_p (mV)
	170	1.1679	1.5719	1.3699	404
	190	1.1589	1.5829	1.3709	424
Ni-POMOF-1000	10	1.2579	1.4149	1.3364	157
	30	1.2299	1.4619	1.3459	232
	50	1.2119	1.4889	1.3504	277
	70	1.1959	1.5109	1.3534	315
	90	1.1829	1.5299	1.3564	347
	110	1.1709	1.5459	1.3584	375
	130	1.1609	1.5639	1.3624	403
	150	1.1499	1.5789	1.3644	429
	170	1.1389	1.5919	1.3654	453
	190	1.1309	1.6069	1.3689	476

Table S13: Comparison of overpotentials of the thermal derivation composites with other studies

Catalyst	Electrolyte	j ($mA\ cm^{-2}$)	Overpotential (mV)	Ref.
Co-POMOF-700	1 M KOH	10	364	this work
Co_2-tzpa	1 M KOH	10	336	[35]
Co-MOF-2	1 M KOH	10	343	[21]
Co@N-CNTF	1 M KOH	10	350	[36]
Co-BTC/CC	1 M KOH	10	370	[37]
rGO/Co_2P-800	1 M KOH	10	378	[38]
Co/Cu-MOF	1 M KOH	10	395	[39]
Ni-POMOF-900	1 M KOH	10	328	this work
CoNi hydroxide UNSs	1 M KOH	10	324	[40]
C@NiCo12	1 M KOH	10	330	[41]
Fe_2O_3@Ni-450	1 M KOH	10	370	[42]
Ni-BTC/CC	1 M KOH	10	390	[37]
UTSA-16	1 M KOH	10	408	[43]

References

[1] C.-L. Wang, C.-Q. Song, W.-H. Shen, Y.-Y. Qi, Y. Xue, Y.-C. Shi, H. Yu, L. Feng, A two-dimensional Ni(II) coordination polymer based on a 3,5-bis(1′,2′,4′-triazol-1′-yl)pyridine ligand for water electro-oxidation, Catal. Sci. Technol. 9 (2019) 1769–1773. doi:10.1039/C9CY00191C.
URL http://dx.doi.org/10.1039/C9CY00191C

[2] J. Sun, T. Zhou, D. Pan, X. Zhang, Y. Wang, Y.-C. Shi, H. Yu, Synthesis, structure, and photoluminescence properties of coordination polymers of 4,4′,4″,4‴-tetrakiscarboxyphenylsilane and 3,5-bis(1′,2′,4′-triazol-1′-yl) pyridine, CrystEngComm 22 (2020) 534–545. doi:10.1039/C9CE01529A.
URL http://dx.doi.org/10.1039/C9CE01529A

[3] Bruker AXS Inc., Madison, Wisconsin, USA, SMART & SAINT Software Reference Manuals, 6th Edition (2003).

[4] G. M. Sheldrick, SADABS: Software for Empirical Absorption Correction, University of Göttingen, 2nd Edition (2002).

[5] G. M. Sheldrick, SHELXTL, Bruker AXS Inc., Madison, Wisconsin, USA, 6th Edition (2001).

[6] Bruker AXS Inc., Madison, Wisconsin, USA, SHELXTL Reference Manual, 6th Edition (2000).

[7] G. M. Sheldrick, *SHELXT* – Integrated space-group and crystal-structure determination, Acta Crystallogr., Sect. A 71 (1) (2015) 3–8. doi:10.1107/S2053273314026370.
URL https://doi.org/10.1107/S2053273314026370

[8] G. M. Sheldrick, Crystal structure refinement with SHELXL, Acta Crystallogr., Sect. C 71 (1) (2015) 3–8. doi:10.1107/S2053229614024218.
URL http://dx.doi.org/10.1107/S2053229614024218

[9] P. Müller, R. Herbst-Irmer, A. L. Spek, T. R. Schneider, M. R. Sawaya, Crystal Structure Refinement: A Crystallographer's Guide to SHELXL, Oxford University Press, Oxford, 2006.

[10] O. V. Dolomanov, L. J. Bourhis, R. J. Gildea, J. A. K. Howard, H. Puschmann, OLEX2: a complete structure solution, refinement and analysis program, J. Appl. Crystallogr. 42 (2) (2009) 339–341. doi:10.1107/S0021889808042726.
URL http://dx.doi.org/10.1107/S0021889808042726

[11] V. A. Blatov, A. P. Shevchenko, D. M. Proserpio, Applied topological analysis of crystal structures with the program package ToposPro, Cryst. Growth Des. 14 (7) (2014) 3576–3586. arXiv:http://dx.doi.org/10.1021/cg500498k, doi:10.1021/cg500498k.
URL http://dx.doi.org/10.1021/cg500498k

[12] K. Bradenburg, Diamond Version 3.1em, Crystal Impact GbR, Bonn, Germany, version 3.1em Edition (2005).

[13] S. Al Sobhi, I. AlShibane, C. R. A. Catlow, A. Daisley, J. S. J. Hargreaves, A. L. Hector, M. D. Higham, C. D. Zeinalipour-Yazdi, A Comparison of the Reactivity of the Lattice Nitrogen in Tungsten Substituted Co_3Mo_3N and Ni_2Mo_3N, ChemSusChem 16 (22) (2023) e202300945. arXiv:https://chemistry-europe.onlinelibrary.wiley.com/doi/pdf/10.1002/cssc.202300945, doi:https://doi.org/10.1002/cssc.202300945.
URL https://chemistry-europe.onlinelibrary.wiley.com/doi/abs/10.1002/cssc.202300945

[14] S. Hund, O. Gómez-Cápiro, H. Ruland, E. M. Heppke, M. Lerch, Ni_2Mo_3N: crystal structure, thermal properties, and catalytic activity for ammonia decomposition, Zeitschrift für Naturforschung B 79 (4) (2024) 147–153. doi:doi:10.1515/znb-2023-0071.
URL https://doi.org/10.1515/znb-2023-0071

[15] K. Maliutina, J. Huang, T. Su, J. Yu, L. Fan, Biomass-derived Ta,N,S co-doped CNTs enriched carbon catalyst for efficient electrochemical oxygen reduction, J. Alloys Compd. 888 (2021) 161479. doi:https://doi.org/10.1016/j.jallcom.2021.161479.
URL https://www.sciencedirect.com/science/article/pii/S0925838821028887

[16] S. I. Moseenkov, V. L. Kuznetsov, N. A. Zolotarev, B. A. Kolesov, I. P. Prosvirin, A. V. Ishchenko, A. V. Zavorin, Investigation of Amorphous Carbon in Nanostructured Carbon Materials (A Comparative Study by TEM, XPS, Raman Spectroscopy and XRD), Materials 16 (3) (2023) 1112. doi:10.3390/ma16031112.
URL https://www.mdpi.com/1996-1944/16/3/1112

[17] B. Fan, H. Wang, H. Zhang, Y. Song, X. Zheng, C. Li, Y. Tan, X. Han, Y. Deng, W. Hu, Phase Transfer of Mo_2C Induced by Boron Doping to Boost Nitrogen Reduction Reaction Catalytic Activity, Adv. Funct. Mater. 32 (20) (2022) 2110783. arXiv:https://onlinelibrary.wiley.com/doi/pdf/10.1002/adfm.202110783, doi:https://doi.org/10.1002/adfm.202110783.
URL https://onlinelibrary.wiley.com/doi/abs/10.1002/adfm.202110783

[18] Y. Guo, Q. Huang, J. Ding, L. Zhong, T.-T. Li, J. Pan, Y. Hu, J. Qian, S. Huang, CoMo carbide/nitride from bimetallic MOF precursors for enhanced OER performance, Int. J. Hydrogen Energy 46 (43) (2021) 22268–22276. doi:https://doi.org/10.1016/j.ijhydene.2021.04.084.
URL https://www.sciencedirect.com/science/article/pii/S0360319921014336

[19] G. Ran, J. Yang, Y. Xing, Y. Zhang, X. Tang, Q. Hu, K. Huang, Z. Zou, H. Yu, X. Xiong, A novel Co_3Mo_3N self-embedded in porous carbon nanocomposite derived

from Mo doped ZIF-67: An effective catalyst for electrochemical H_2O_2 sensing, Microchem. J. 185 (2023) 108296. doi:https://doi.org/10.1016/j.microc.2022.108296.
URL https://www.sciencedirect.com/science/article/pii/S0026265X22011249

[20] M. S. Hamdan, Riyanto, M. R. Othman, Preparation and characterization of nano size niooh by direct electrochemical oxidation of nickel plate, Int. J. Electrochem. Sci. 8 (2013) 4747–4760.
URL http://www.electrochemsci.org/papers/vol8/80404747.pdf

[21] P. Muthukumar, G. Arunkumar, M. Pannipara, A. G. Al-Sehemi, D. Moon, S. P. Anthony, Enhancing the electrocatalytic OER activity of Co-MOFs through labile solvents coordination, New J. Chem. 47 (2023) 20831–20837. doi:10.1039/D3NJ03660J.
URL http://dx.doi.org/10.1039/D3NJ03660J

[22] T. Cao, Y. Li, T. Xie, X. Wang, Z. Huang, H. Yu, Synthesis, structures and electrocatalytic properties of coordination polymers of 4,4′,4″,4‴-tetrakiscarboxyphenylsilane and 1,3,5-tris(2-methyl-1*H*-imidazol-1-yl)benzene, CrystEngComm 26 (2024) 985–994. doi:10.1039/D3CE01266B.
URL http://dx.doi.org/10.1039/D3CE01266B

[23] W. Zheng, *iR* Compensation for Electrocatalysis Studies: Considerations and Recommendations, ACS Energy Lett. 8 (4) (2023) 1952–1958. arXiv:https://doi.org/10.1021/acsenergylett.3c00366, doi:10.1021/acsenergylett.3c00366.
URL https://doi.org/10.1021/acsenergylett.3c00366

[24] L. Zhang, T. Mi, M. A. Ziaee, L. Liang, R. Wang, Hollow POM@MOF hybrid-derived porous $Co_3O_4/CoMoO_4$ nanocages for enhanced electrocatalytic water oxidation, J. Mater. Chem. A 6 (2018) 1639–1647. doi:10.1039/C7TA08683K.
URL http://dx.doi.org/10.1039/C7TA08683K

[25] T. Shinagawa, A. T. Garcia-Esparza, K. Takanabe, Insight on Tafel slopes from a microkinetic analysis of aqueous electrocatalysis for energy conversion, Sci. Rep. 5 (2015) 13801. doi:10.1038/srep13801.
URL https://www.nature.com/articles/srep13801

[26] N.-T. Suen, S.-F. Hung, Q. Quan, N. Zhang, Y.-J. Xu, H. M. Chen, Electrocatalysis for the oxygen evolution reaction: recent development and future perspectives, Chem. Soc. Rev. 46 (2017) 337–365. doi:10.1039/C6CS00328A.
URL http://dx.doi.org/10.1039/C6CS00328A

[27] O. van der Heijden, S. Park, R. E. Vos, J. J. J. Eggebeen, M. T. M. Koper, Tafel slope plot as a tool to analyze electrocatalytic reactions, ACS Energy Lett. 9 (4) (2024) 1871–1879. arXiv:https://doi.org/10.1021/acsenergylett.4c00266, doi:10.1021/acsenergylett.4c00266.
URL https://doi.org/10.1021/acsenergylett.4c00266

[28] W. Wu, Q. Lu, G. Li, Y. Wang, How to extract kinetic information from Tafel analysis in electrocatalysis, J. Chem. Phys. 159 (22) (2023) 221501. arXiv:https://pubs.aip.org/aip/jcp/article-pdf/doi/10.1063/5.0175156/19848719/221501_1_5.0175156.pdf, doi:10.1063/5.0175156.
URL https://doi.org/10.1063/5.0175156

[29] Z. Ren, S. Wang, J. Yu, F. Mao, K. Wang, H. Wu, Cu/MoO_2 Schottky heterojunction derived from a new designed POMOFs in-situ as high efficient electrocatalysts for hydrogen evolution reaction in universal-pH electrolytes and seawater, Chem. Eng. J. 470 (2023) 144107. doi:https://doi.org/10.1016/j.cej.2023.144107.
URL https://www.sciencedirect.com/science/article/pii/S1385894723028383

[30] W. Zheng, M. Liu, L. Y. S. Lee, Electrochemical instability of metal–organic frameworks: In situ spectroelectrochemical investigation of the real active sites, ACS Catal. 10 (1) (2020) 81–92. arXiv:https://doi.org/10.1021/acscatal.9b03790, doi:10.1021/acscatal.9b03790.
URL https://doi.org/10.1021/acscatal.9b03790

[31] J. J. Van Benschoten, J. Y. Lewis, W. R. Heineman, D. A. Roston, P. T. Kissinger, Cyclic voltammetry experiment, J. Chem. Educ. 60 (9) (1983) 772–776. arXiv:https://doi.org/10.1021/ed060p772, doi:10.1021/ed060p772.
URL https://doi.org/10.1021/ed060p772

[32] N. Elgrishi, K. J. Rountree, B. D. McCarthy, E. S. Rountree, T. T. Eisenhart, J. L. Dempsey, A practical beginner's guide to cyclic voltammetry, J. Chem. Educ. 95 (2) (2018) 197–206. arXiv:https://doi.org/10.1021/acs.jchemed.7b00361, doi:10.1021/acs.jchemed.7b00361.
URL https://doi.org/10.1021/acs.jchemed.7b00361

[33] S. Tanimoto, A. Ichimura, Discrimination of inner- and outer-sphere electrode reactions by cyclic voltammetry experiments, J. Chem. Educ. 90 (6) (2013) 778–781. arXiv:https://doi.org/10.1021/ed200604m, doi:10.1021/ed200604m.
URL https://doi.org/10.1021/ed200604m

[34] L. Trotochaud, S. L. Young, J. K. Ranney, S. W. Boettcher, Nickel–iron oxyhydroxide oxygen-evolution electrocatalysts: The role of intentional and incidental iron incorporation, J. Am. Chem. Soc. 136 (18) (2014) 6744–6753. arXiv:https://doi.org/10.1021/ja502379c, doi:10.1021/ja502379c.
URL https://doi.org/10.1021/ja502379c

[35] N. Liu, Q. Zhang, J. Guan, A binuclear co-based metal–organic framework towards efficient oxygen evolution reaction, Chem. Commun. 57 (2021) 5016–5019. doi:10.1039/D1CC01492G.
URL http://dx.doi.org/10.1039/D1CC01492G

[36] H. Guo, Q. Feng, J. Zhu, J. Xu, Q. Li, S. Liu, K. Xu, C. Zhang, T. Liu, Cobalt nanoparticle-embedded nitrogen-doped carbon/carbon nanotube frameworks derived from a metal–organic framework for tri-functional ORR, OER and HER electrocatalysis, J. Mater. Chem. A 7 (2019) 3664–3672. doi:10.1039/C8TA11400E.
URL http://dx.doi.org/10.1039/C8TA11400E

[37] S. Naik Shreyanka, J. Theerthagiri, S. J. Lee, Y. Yu, M. Y. Choi, Multiscale design of 3D metal–organic frameworks (M–BTC, M: Cu, Co, Ni) via PLAL enabling bifunctional electrocatalysts for robust overall water splitting, Chem. Eng. J. 446 (2022) 137045. doi:https://doi.org/10.1016/j.cej.2022.137045.
URL https://www.sciencedirect.com/science/article/pii/S1385894722025372

[38] X. Zhao, Y. Fan, H. Wang, C. Gao, Z. Liu, B. Li, Z. Peng, J.-H. Yang, B. Liu, Cobalt phosphide-embedded reduced graphene oxide as a bifunctional catalyst for overall water splitting, ACS Omega 5 (12) (2020) 6516–6522. arXiv:https://doi.org/10.1021/acsomega.9b04143, doi:10.1021/acsomega.9b04143.
URL https://doi.org/10.1021/acsomega.9b04143

[39] Q. Qiu, T. Wang, L. Jing, K. Huang, D. Qin, Tetra-carboxylic acid based metal-organic framework as a high-performance bifunctional electrocatalyst for HER and OER, Int. J. Hydrogen Energy 45 (19) (2020) 11077–11088. doi:https://doi.org/10.1016/j.ijhydene.2020.02.033.
URL https://www.sciencedirect.com/science/article/pii/S0360319920305152

[40] K. He, Z. Cao, R. Liu, Y. Miao, H. Ma, Y. Ding, *Insitu* decomposition of metal–organic frameworks into ultrathin nanosheets for the oxygen evolution reaction, Nano Res. 9 (6) (2016) 1856–1865. doi:10.1007/s12274-016-1078-x.
URL https://doi.org/10.1007/s12274-016-1078-x

[41] S. Tan, W. Ouyang, Y. Ji, Q. Hong, Carbon wrapped bimetallic NiCo nanospheres toward excellent HER and OER performance, J. Alloys Compd. 889 (2021) 161528. doi:https://doi.org/10.1016/j.jallcom.2021.161528.
URL https://www.sciencedirect.com/science/article/pii/S0925838821029376

[42] C. Stienen, G. Bendt, Direct mocvd growth of iron oxide on three-dimensional nickel foam as electrode for the oxygen evolution reaction, ChemSusChem 13 (22) (2020) 5954–5961. arXiv:https://chemistry-europe.onlinelibrary.wiley.com/doi/pdf/10.1002/cssc.202001896, doi:https://doi.org/10.1002/cssc.202001896.
URL https://chemistry-europe.onlinelibrary.wiley.com/doi/abs/10.1002/cssc.202001896

[43] J. Jiang, L. Huang, X. Liu, L. Ai, Bioinspired cobalt–citrate metal–organic framework as an efficient electrocatalyst for water oxidation, ACS Appl. Mater. Interfaces 9 (8) (2017) 7193–7201. arXiv:http://dx.doi.org/10.1021/acsami.6b16534, doi:10.1021/acsami.6b16534.
URL http://dx.doi.org/10.1021/acsami.6b16534